(12) INTERNATIONAL APPLICATION PUBLISHED UNDER THE PATENT COOPERATION TREATY (PCT)

(19) World Intellectual Property Organization
International Bureau

(43) International Publication Date
19 December 2024 (19.12.2024)

WIPO | PCT

(10) International Publication Number
WO 2024/259008 A2

(51) International Patent Classification:
Not classified

(21) International Application Number:
PCT/US2024/033668

(22) International Filing Date:
12 June 2024 (12.06.2024)

(25) Filing Language: English

(26) Publication Language: English

(30) Priority Data:
63/507,683 12 June 2023 (12.06.2023) US

(71) Applicant: **WASHINGTON UNIVERSITY** [US/US]; One Brookings Drive, CB8013, St. Louis, Missouri 63130 (US).

(72) Inventors: **LEUTHARDT, Eric**; One Brookings Drive, CB8013, St. Louis, Missouri 63130 (US). **PARK, Ki Yun**; One Brookings Drive, CB8013, St. Louis, Missouri 63130 (US). **SNYDER, Abraham**; One Brookings Drive, CB8013, St. Louis, Missouri 63130 (US).

(74) Agent: **MCCAY, Michael**; One Brookings Drive, CB8013, St. Louis, Missouri 63130 (US).

(81) Designated States *(unless otherwise indicated, for every kind of national protection available)*: AE, AG, AL, AM, AO, AT, AU, AZ, BA, BB, BG, BH, BN, BR, BW, BY, BZ, CA, CH, CL, CN, CO, CR, CU, CV, CZ, DE, DJ, DK, DM, DO, DZ, EC, EE, EG, ES, FI, GB, GD, GE, GH, GM, GT, HN, HR, HU, ID, IL, IN, IQ, IR, IS, IT, JM, JO, JP, KE, KG, KH, KN, KP, KR, KW, KZ, LA, LC, LK, LR, LS, LU, LY, MA, MD, MG, MK, MN, MU, MW, MX, MY, MZ, NA, NG, NI, NO, NZ, OM, PA, PE, PG, PH, PL, PT, QA, RO, RS, RU, RW, SA, SC, SD, SE, SG, SK, SL, ST, SV, SY, TH, TJ, TM, TN, TR, TT, TZ, UA, UG, US, UZ, VC, VN, WS, ZA, ZM, ZW.

(84) Designated States *(unless otherwise indicated, for every kind of regional protection available)*: ARIPO (BW, CV, GH, GM, KE, LR, LS, MW, MZ, NA, RW, SC, SD, SL, ST, SZ, TZ, UG, ZM, ZW), Eurasian (AM, AZ, BY, KG, KZ, RU, TJ, TM), European (AL, AT, BE, BG, CH, CY, CZ, DE, DK, EE, ES, FI, FR, GB, GR, HR, HU, IE, IS, IT, LT, LU, LV, MC, ME, MK, MT, NL, NO, PL, PT, RO, RS, SE, SI, SK, SM, TR), OAPI (BF, BJ, CF, CG, CI, CM, GA, GN, GQ, GW, KM, ML, MR, NE, SN, TD, TG).

Published:
— *without international search report and to be republished upon receipt of that report (Rule 48.2(g))*

(54) Title: BRAIN PROGNOSIS SYSTEMS AND METHODS OF USE THEREOF

(57) Abstract: Among the various aspects of the present disclosure is the provision of systems and methods of use for identifying brain disorders and pathological neurometabolic aging based on the frequency-based analysis of functional MRI imaging data.

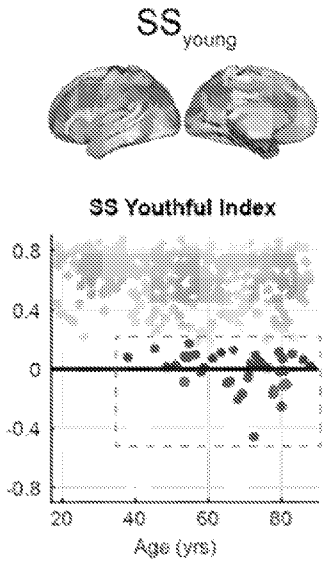

FIG. 14A

WO 2024/259008 A2

TITLE OF THE INVENTION

BRAIN PROGNOSIS SYSTEMS AND METHODS OF USE THEREOF

CROSS-REFERENCE TO RELATED APPLICATIONS

This application claims the benefit of priority to U.S. Provisional Application Serial No. 63/507,683 filed on June 12, 2023, which is incorporated herein by reference in its entirety.

STATEMENT REGARDING FEDERALLY SPONSORED RESEARCH OR DEVELOPMENT

This invention was made with government support under CA203861 awarded by the National Institutes of Health. The government has certain rights in the invention.

MATERIAL INCORPORATED-BY-REFERENCE

Not applicable.

FIELD OF THE INVENTION

The present disclosure generally relates to brain prognostic systems and methods of use thereof.

BACKGROUND OF THE INVENTION

Glioblastomas, a highly aggressive form of brain cancer, are a brain-wide disease. Glioblastomas exhibit markedly altered metabolism that sustains and expands the tumor microenvironment. Accordingly, cerebrospinal fluid (CSF) metabolomic studies demonstrate significant differences between tumor patients and healthy controls. Importantly, glioma cells and glioma stem-like cells efficiently employ metabolic strategies that induce changes beyond the tumor microenvironment. The products of this altered metabolism promote neovascularization and a tolerogenic environment. Newly synthesized blood and lymph vessels facilitate the exchange of metabolites between the tumor and the parenchymal macroenvironment: oxygen and nutrients are delivered to the tumor and soluble factors are released from the tumor into the bloodstream. These findings raise the question of whether the global metabolic effects of

glioblastoma can be quantified and, if so, whether they carry prognostic significance.

Functional magnetic resonance imaging (fMRI) studies using resting-state (rs-fMRI) enables brain-wide monitoring of regional metabolic and blood-oxygen activity using blood-oxygen level-dependent (BOLD) signals, which spontaneously fluctuate over tens of seconds (i.e., infra-slow activity) at a millimeter scale resolution. Most studies that use rs-fMRI to study gliomas have employed functional connectivity (FC), which measures the Pearson temporal correlation between BOLD signals extracted from pre-determined regions of interest. These studies have demonstrated that brain-wide changes in resting-state FC extend beyond the anatomical limits of the tumor and often involve an attenuation in global FC strength.

Factors that can affect the correlation between two signals include signal similarity and the signal-to-noise ratio. Accordingly, to gain insights into the underlying mechanisms of FC changes in tumor patients, we need to utilize a range of techniques for studying BOLD signals. These methods include computing the power-law exponent, β, of the scale-free fMRI signals and fractional amplitude of low-frequency fluctuation (fALFF), which evaluates the ratio of the total power in the low-frequency to all measurable frequencies. Studies have shown that the power-law exponent of the scale-free fMRI signals correlates with a cerebral metabolic rate for glucose (CMRGlu). Moreover, the simultaneous acquisition of rs-fMRI and FDG-PET reveals regionally specific correlations between fALFF and CMRGlu. Thus, frequency domain analysis provides a complementary perspective on brain function distinct from connectivity analysis. fALFF and power-law estimation both enable quantification of focal neural activity over the whole brain and, hence are ideally suited to the investigation of the global effects of glioblastoma tumors.

Additionally, brain metabolism and measures of physiologic integrity decline with age in a manner parallel to numerous other physiologic measures. This principle has been demonstrated with Positron Emission Tomography (PET) as well as rs-fMRI. Cerebral metabolism and blood flow globally decline with advancing age. This decline is not uniform across different brain regions; it

differentially affects regions with varying brain metabolism. Specifically, the regional pattern of cerebral metabolism diverges from the normative youthful pattern. Intriguingly, some older adults retain youthful metabolic patterns while others do not.

rs-fMRI studies of aging have largely focused on FC, which correlates BOLD signals in functionally related regions known as resting state networks (RSNs). Comparatively fewer studies have evaluated age-related changes in the statistics of local spontaneous BOLD signals. These studies have employed a variety of metrics including the amplitude of low-frequency fluctuations (ALFF), BOLD signal variability, and BOLD fluctuation amplitude, all of which relate to the temporal variance of BOLD fMRI signals. Recent results demonstrate that developmental trajectories of ALFF in a cohort aged 8 to 18 years are topographically organized in relation to the sensorimotor-association cortex axis. In parallel, aging studies have demonstrated reduced signal variance and less between-region variability in old as compared to young adults. However, these previous reports generally do not consider the spectral characteristics of BOLD fMRI signals.

BOLD fluctuations are 1/f-like, i.e., characterized by an approximately linear decrease in log spectral power with increasing frequency. Spectral characteristics of BOLD signals have been measured using spectral slope either in log-log (i.e., power-law exponent) or log-linear plots, autocorrelation function, and fALFF, which is distinct from ALFF as it quantifies the fraction of power in the lowest frequencies. Thus, fALFF captures a spectral characteristic comparable to the spectral slope. Importantly, the spectral properties of resting-state BOLD signals vary across brain networks, depending on the task state, relate to brain tumors and clinical comorbidities, and correlate with brain glucose metabolism. In particular, cortical regions exhibiting slower intrinsic dynamics are associated with higher glucose metabolism.

SUMMARY OF THE INVENTION

Among the various aspects of the present disclosure is the provision of systems and methods of use for brain prognosis.

Briefly, therefore, the present disclosure is directed to brain cancer and aging prognosis systems and methods of use thereof.

In one aspect, a system to identify a brain disorder in a patient that includes at least one processor is disclosed. The at least one processor is configured to: receive a resting-state functional magnetic resonance image (rs-fMRI) dataset obtained from a brain of the patient; transform the rs-fMRI data set into a power spectral density (PSD) dataset; transform at least a portion of the PSD dataset corresponding to at least one region of the brain of the subject into a power-law exponent (β) dataset and at least two fractional amplitudes of low-frequency fluctuations (fALFF) datasets; compare the power-law exponent (β) dataset and at least two fALFF datasets to corresponding reference power-law exponent (β) datasets and at least two reference fALFF datasets obtained from healthy control subjects; identify the brain disorder based on differences in the power-law exponent (β) dataset and at least two fALFF datasets relative to the corresponding reference power-law exponent (β) dataset and at least two reference fALFF datasets; and communicate the brain disorder to a display device of a practitioner. The at least two aALFF datasets are selected from a lower-frequency fALFF dataset computed from a lower-frequency portion of the PSD dataset and a higher-frequency fALFF computed from a higher-frequency portion of the PSD dataset, or a fALFF dataset computed from all frequencies of the PSD dataset. In some aspects, the rs-fMRI dataset includes a plurality of time-series of blood-oxygen-level-dependent (BOLD) signals, and each time-series is obtained from a voxel within the brain of the subject. In some aspects, the PSD dataset includes a series of spectral powers and corresponding BOLD signal frequencies over a pre-specified range of BOLD signal frequencies for each voxel of the rs-fMRI dataset. In some aspects, the power-law exponent (β) dataset includes a plurality of power-law exponents (β) corresponding to the plurality of voxels of the rs-fMRI dataset, and each power-law exponent (β) is obtained by fitting a power-law function to each PSD of at least a portion of the PSD dataset. In some aspects, the pre-specified range of BOLD signal frequencies includes a range of less than about 0.100 Hz. In some aspects, the pre-specified range of BOLD signal frequencies includes a range from about 0.025 Hz to about 0.105 Hz. In some aspects, the brain disorder is identified in

the patient for the differences including at least one of: power-law exponents (β) lower than the corresponding reference power-law exponents (β); fALFFs over ranges of BOLD signal frequencies of less than about 100 Hz are lower than the corresponding reference fALFFs; and fALFFs over a range of BOLD signal frequencies from about 0.025 Hz to about 0.105 Hz are lower than the corresponding reference fALFFs. In some aspects, the processor is further configured to: calculate a predicted prognosis for the subject based on the differences in the at least one fALFF dataset relative to a corresponding at least one reference fALFF dataset; and communicate the predicted prognosis to the display device of the practitioner. In some aspects, the predicted prognosis of a shortened survival probability is calculated for at least one of: the fALFF dataset obtained from a lower-frequency range of BOLD signal frequencies from about 0.025 Hz to about 0.045 Hz is lower than the corresponding reference fALFF dataset; and the fALFF dataset obtained from a higher-frequency range of BOLD signal frequencies from about 0.085 Hz to about 1.05 Hz is higher than the corresponding reference fALFF dataset.

In another aspect, a computer-implemented method to identify a brain disorder in a patient is disclosed that includes: receiving a resting-state functional magnetic resonance image (rs-fMRI) dataset obtained from a brain of the patient; transforming the rs-fMRI data set into a power spectral density (PSD) dataset; transforming at least a portion of the PSD dataset corresponding to at least one region of the brain of the subject into a power-law exponent (β) dataset and at least two fractional amplitudes of low-frequency fluctuations (fALFF) datasets; comparing the power-law exponent (β) dataset and at least two fALFF datasets to corresponding reference power-law exponent (β) datasets and at least two reference fALFF datasets obtained from healthy control subjects; identifing the brain disorder based on differences in the power-law exponent (β) dataset and at least two fALFF datasets relative to the corresponding reference power-law exponent (β) dataset and at least two reference fALFF datasets; and

communicate the brain disorder to a display device of a practitioner. The at least two aALFF datasets are selected from a lower-frequency fALFF dataset computed from a lower-frequency portion of the PSD dataset and a higher-frequency fALFF computed from a higher-frequency portion of the PSD dataset,

or a fALFF dataset computed from all frequencies of the PSD dataset. In some aspects, the rs-fMRI dataset includes a plurality of time-series of blood-oxygen-level-dependent (BOLD) signals, each time-series obtained from a voxel within the brain of the subject. In some aspects, the PSD data set includes a series of spectral powers and corresponding BOLD signal frequencies over a pre-specified range of BOLD signal frequencies for each voxel of the rs-fMRI dataset. In some aspects, the power-law exponent (β) dataset includes a plurality of power-law exponents (β) corresponding to the plurality of voxels of the rs-fMRI dataset, each power-law exponent (β) obtained by fitting a power-law function to each PSD of at least a portion of the PSD dataset. In some aspects, the pre-specified range of BOLD signal frequencies includes a range of less than about 0.100 Hz. In some aspects, the pre-specified range of BOLD signal frequencies includes a range from about 0.025 Hz to about 0.105 Hz. In some aspects, the brain disorder is identified in the patient for the differences including at least one of: power-law exponents (β) lower than the corresponding reference power-law exponents (β); fALFFs over a range of BOLD signal frequencies of less than about 100 Hz are lower than the corresponding reference fALFFs; and fALFFs over a range of BOLD signal frequencies from about 0.025 Hz to about 0.105 Hz are higher than the corresponding reference fALFFs. In some aspects, the processor is further configured to calculate a predicted prognosis for the subject based on the differences in the at least one fALFF dataset to corresponding at least one reference fALFF dataset. In some aspects, the predicted prognosis includes a shortened survival probability is calculated for at least one of: the fALFF dataset obtained from the lower-frequency range of BOLD signal frequencies from about 0.025 Hz to about 0.045 Hz is lower than the corresponding reference fALFF dataset; and the fALFF dataset obtained from the higher-frequency range of BOLD signal frequencies from about 0.085 Hz to about 1.05 Hz is higher than the corresponding reference fALFF dataset.

In another aspect, a system to identify pathological neurometabolic aging in a patient is disclosed that includes at least one processor configured to: receive a resting-state functional magnetic resonance image (rs-fMRI) dataset obtained from a brain of the patient; transform the rs-fMRI data set into a power spectral density (PSD) dataset; transform at least a portion of the PSD dataset

corresponding to at least one region of the brain of the subject into a spectral slope (SS) dataset; compare the SS dataset to a corresponding reference SS dataset obtained from age-matched healthy control subjects; identify the pathological neurometabolic aging based on differences in the SS dataset relative to the corresponding reference SS dataset; and communicate the pathological neurometabolic aging to a practitioner. In some aspects, the rs-fMRI dataset includes a plurality of time-series of blood-oxygen-level-dependent (BOLD) signals, each time-series obtained from a voxel within the brain of the subject. In some aspects, the PSD data set includes a series of spectral powers and corresponding BOLD signal frequencies over a pre-specified range of BOLD signal frequencies for each voxel of the rs-fMRI dataset. In some aspects, the SS dataset includes a plurality of spectral slopes corresponding to the plurality of voxels of the rs-fMRI dataset, each spectral slope including a negative slope of a linear regression of log power against frequency from each PSD of the PSD dataset. In some aspects, the at least one processor is further configured to transform the SS dataset and the corresponding reference dataset into an SS Youthful Index, the SS Youthful Index including a Spearman's correlation between the SS dataset and the corresponding reference SS dataset over a pre-specified range of BOLD signal frequencies. In some aspects, the pathological neurometabolic aging is identified if the SS Youthful Index falls below a threshold value. In some aspects, the threshold value includes a value of an SS Youthful Index at least three scaled median absolute deviations from a median value of SS Youthful Indices obtained for a healthy control population. In some aspects, the pre-specified range of BOLD signal frequencies includes a range from about 0.015 HZ to about 0.145 Hz.

In another aspect, a computer-implemented method to identify pathological neurometabolic aging in a patient is disclosed that includes: receiving a resting-state functional magnetic resonance image (rs-fMRI) dataset obtained from a brain of the patient; transforming the rs-fMRI data set into a power spectral density (PSD) dataset; transforming at least a portion of the PSD dataset corresponding to at least one region of the brain of the subject into a spectral slope (SS) dataset; comparing the SS dataset to a corresponding reference SS dataset obtained from age-matched healthy control subjects;

identifying the pathological neurometabolic aging based on differences in the SS dataset and the corresponding reference SS dataset; and communicating the pathological neurometabolic aging to a display device of a practitioner. In some aspects, the rs-fMRI dataset includes a plurality of time-series of blood-oxygen-level-dependent (BOLD) signals, each time-series obtained from a voxel within the brain of the subject. In some aspects, the PSD data set includes a series of spectral powers and corresponding BOLD signal frequencies over a pre-specified range of BOLD signal frequencies for each voxel of the rs-fMRI dataset. In some aspects, the SS dataset includes a plurality of spectral slopes corresponding to the plurality of voxels of the rs-fMRI dataset, each spectral slope including a negative slope of a linear regression of log power against frequency from each PSD of the PSD dataset. In some aspects, the method further includes transforming the SS dataset and the corresponding reference dataset into an SS Youthful Index, the SS Youthful Index including a Spearman's correlation between the SS dataset and the corresponding reference SS dataset over a pre-specified range of BOLD signal frequencies. In some aspects, the method further includes identifying the pathological neurometabolic aging based on differences in the SS dataset and the corresponding reference SS dataset. In some aspects, the method further includes identifying the pathological neurometabolic aging if the SS Youthful Index falls below a threshold value. In some aspects, the threshold value includes a value of the SS Youthful Index at least three scaled median absolute deviations from a median value of the SS Youthful Index obtained for a healthy control population. In some aspects, the pre-specified range of BOLD signal frequencies includes a range from about 0.015 HZ to about 0.145 Hz.

Other objects and features will be in part apparent and in part pointed out hereinafter.

DESCRIPTION OF THE DRAWINGS

Those of skill in the art will understand that the drawings, described below, are for illustrative purposes only. The drawings are not intended to limit the scope of the present teachings in any way.

FIG. 1 is a block diagram schematically illustrating a system in

accordance with one aspect of the disclosure.

FIG. 2 is a block diagram schematically illustrating a computing device in accordance with one aspect of the disclosure.

FIG. 3 is a block diagram schematically illustrating a remote or user computing device in accordance with one aspect of the disclosure.

FIG. 4 is a block diagram schematically illustrating a server system in accordance with one aspect of the disclosure.

FIG. 5A is a postcontrast T1w image of an exemplary glioblastoma patient.

FIG. 5B contains the images of FIG. 5A segmented to identify the following: vasogenic edema (green), necrotic/non-enhancing tumor core (yellow), and enhancing tumor core (red).

FIG. 5C is an exemplary tumor frequency heatmap showing the distribution of contrast-enhanced tumor volume in all 189 subjects of the example cohort; the intensity of the color scale represents the number of patients, ranging from 0 to 20.

FIG. 6A contains maps of the averaged voxel-wise β obtained in the OASIS subjects and glioblastoma patient dataset. Red hues indicate a relatively steeper slope, i.e., more power at low frequencies; blue hues indicate a relatively flatter slope.

FIG. 6B contains fMRI signal power spectra (mean ± standard deviation) computed for the gray matter cortical (left), gray matter sub-cortical (middle), and white matter (right) for each subject in each group (black = reference subjects dataset; red = patient dataset) and averaged across the subjects. Spectra computed at all three regions were significantly different between the two groups.

FIG. 6C is a graph of averaged β across 5 subcortical regions (amygdala, hippocampus, thalamus, dorsal and ventral striatum) and 8 cortical regions in the OASIS dataset and glioblastoma patient dataset. Abbreviations: amygdala (Amyg), hippocampus (Hp), thalamus (Thal), dorsal striatum (DS), ventral striatum (VS), cingulo-opercular network (CON), salience network (Sal),

somatomotor network (SMN), ventral attention network (VAN), dorsal attention network (DAN), default mode network (DMN), fronto-parietal network (FPN), visual network (VIS), gray matter (GM), white matter (WM). ** ($p < 0.0001$).

FIG. 7A contains maps of fALFF topography computed within the frequency band, 0.03 – 0.10Hz; fALFF topography averaged across the subjects in each group at an identified frequency is shown at left and averaged frequency-specific fALFF in the gray matter cortical ROIs and white matter across subjects in each group is shown at right. Abbreviations: reference OASIS subjects dataset (REF), patient dataset (PAT). ** ($p < 0.0001$).

FIG. 7B contains maps of fALFF topography computed for a 0.03Hz fALFF frequency; fALFF topography averaged across the subjects in each group at an identified frequency is shown at left and averaged frequency-specific fALFF in the gray matter cortical ROIs and white matter across subjects in each group is shown at right. Abbreviations: reference OASIS subjects dataset (REF), patient dataset (PAT). ** ($p < 0.0001$).

FIG. 7C contains maps of fALFF topography computed for a 0.06Hz fALFF frequency; fALFF topography averaged across the subjects in each group at an identified frequency is shown at left and averaged frequency-specific fALFF in the gray matter cortical ROIs and white matter across subjects in each group is shown at right. Abbreviations: reference OASIS subjects dataset (REF), patient dataset (PAT). ** ($p < 0.0001$).

FIG. 7D contains maps of fALFF topography computed for a 0.10Hz fALFF frequency; fALFF topography averaged across the subjects in each group at an identified frequency is shown at left and averaged frequency-specific fALFF in the gray matter cortical ROIs and white matter across subjects in each group is shown at right. Abbreviations: reference OASIS subjects dataset (REF), patient dataset (PAT). ** ($p < 0.0001$).

FIG. 8A contains maps of averaged voxel-wise power-law exponents obtained in the unmethylated and methylated MGMT groups.

FIG. 8B contains fMRI signal power spectra averaged across the subjects in each group (mean ± standard error of the mean). Frequency-specific fALFF maps are divided based on where the two groups cross over at the

corresponding frequency bands.

FIG. 8C contains maps of lower-fALFF and higher-fALFF maps of glioblastoma patients based on the tumor's MGMT promoter methylation status. Warm hues, compared to cool hues, indicate an increased contribution of the frequency band to the power spectra.

FIG. 9A is a histogram summarizing the comorbidities of patients selected as described below. Patients were ranked based on their averaged power-law exponent in the cortical gray matter voxels, and the top 20% of patients with smaller β and greater β were selected. In each group, we computed the percentage of patients with the corresponding comorbid conditions shown on the left of the bar. There was generally a greater percentage of patients with smaller β (white-gray bars) with comorbid conditions than those with greater β (red bars).

FIG. 9B is a graph of averaged gray-matter cortical β as a function of the number of comorbidities as determined from the analysis described in FIG. 9A. For each patient, we compared their averaged gray-matter cortical β to their number of comorbidities shown in FIG. 9A. There was a significant negative correlation between the number of comorbidities patients presented and their averaged β ($p < 0.005$). Abbreviations: deep vein thrombosis (DVT), pulmonary embolism (PE), chronic kidney disease (CKD), hyperlipidemia (HLD), hypertension (HTN), presented with at the time of evaluation (Pw), history (Hx).

FIG. 10A is an MRI signal power spectra power obtained as described below. Patients were median split into two groups based on their overall survival (OS), and fMRI signal power spectra were averaged across the subjects in each group (mean ± standard error of the mean). Patients with greater OS had greater gray matter fALFF in the lowest frequency band (0.025-0.45Hz), comparable in the middle-frequency band (0.045-0.085Hz), and a smaller fALFF in the highest frequency band (0.085-0.105Hz).

FGI. 10B is a graph summarizing voxel-wise % difference between the fALFF maps in each frequency band (0.025-0.045; 0.045-0.085; 0.085-0.105Hz) between the two groups described in FIG. 10A, determined according to the following equation:

$\frac{fALFF_{OS>14m} - fALFF_{OS\leq 14m}}{fALFF_{OS\leq 14m}}$.

FIG. 10C contains maps of averaged fALFF in three frequency bands in each group based on their OS group as described in FIG. 10A. Warm hues, compared to cool hues, indicate an increased relative power in the corresponding frequency band.

FIG. 10D contains Kaplan-Meier survival graphs comparing OS of glioblastoma patients with low and high fALFF, based on the analysis from FIG. 10C.

FIG. 11A is a schematic of two distinct BOLD fluctuations, samples from the same ROIs in two subjects, shown in both time and frequency domains.

FIG. 11B is a set of graphs of (left) averaged power spectra and frequency across participants within three age groups and (right) averaged power spectra and frequency demonstrated by a logged power as a function of frequency. Spectral slope (SS) is defined as the negative of the first derivative of the slope fitted to the logged power.

FIG. 11C contains parcellated SS maps, averaged across participants within three age groups, illustrating the spatial patterning of age-related SS flattening across the lifespan. Cortical regions with steep spectral slopes include medial and lateral parietal, prefrontal, posterior cingulate, and visual cortices (note warmer hues). The age cohorts include 20-40 years (n = 113), 41-65 years (n = 179), and 66-87 years (n = 163). Although age-related SS flattening occurs across cortical regions, the characteristic features of SS topography persist across all age groups.

FIG. 12A is an image of the patterning of age effects on the SS (age-specific R^2) across the cortical surface.

FIG. 12B is a map of parcellated cerebral metabolic rate of glucose use (CMRGlc) averaged across 30 cognitively unimpaired young adults aged 25-45 years (AMBR dataset).

FIG. 12C is a graph of Spearman's correlation between age-specific R^2 and average CMRGlc map. Age-specific R^2 correlates with CMRGlc. Each dot represents each parcel.

FIG. 13A is an image and graph of trajectories of age-related SS flattening across cortical parcels, identified by fuzzy c-means clustering. Cluster 1, comprising the majority of cortical parcels, exhibits a consistent flattening of the spectral slope with age.

FIG. 13B is an image and graph of trajectories of age-related SS flattening across cortical parcels, identified by fuzzy c-means clustering. Cluster 2 includes a select set of cortical parcels with spatial topography akin to the auditory, cingulo-opercular, and salience networks, showing a delayed flattening that begins in mid-adulthood (~50 yrs).

FIG. 13C is an image and graph of the ratio of the voxels within each RSN (illustrated in the inset) showing a thresholded probabilistic RSN map that belongs to either Cluster 1 (FIG.13A) or Cluster 2 (FIG. 13B). Values greater than 1 indicate more RSN voxels in Cluster 2; values closer to 0 suggest more RSN voxels in Cluster 1.

FIG. 14A is a (top) map of topography of average spectral slope (SS) and (bottom) a corresponding graph. SS_{young} map was computed by averaging SS maps of younger participants (<45 yrs) in the CamCAN dataset. (Bottom) Each dot (grey and red) represents an individual's Spearman's correlation between their SS map and CamCAN-average SS_{young} map (SS Youthful Index). The dashed box outlines red dots, identifying outliers whose correlation values are greater than 3 scaled median absolute deviations from the median.

FIG. 14B is a (top) map of topography of average CMRGlc and (bottom) a corresponding graph. The $CMRglc_{young}$ map was generated from the AMBR dataset. (Bottom) Each dot (grey and red) represents an individual's Spearman's correlation between their SS map and AMBR-average $CMRGlc_{young}$ map. The dashed box outlines red dots, identifying outliers whose correlation values are greater than 3 scaled median absolute deviations from the median.

FIG. 14C is a (top) map of the topography of average CMRO2 and (bottom) a corresponding graph. $CMRO2_{young}$ map was generated from the AMBR dataset. (Bottom) Each dot (grey and red) represents an individual's Spearman's correlation between their SS map and AMBR-average $CMRO2_{young}$ map. The dashed box outlines red dots, identifying outliers whose correlation

values are greater than 3 scaled median absolute deviations from the median.

FIG. 14D is a (top) map of topography of average CMRO2 and (bottom) a corresponding graph. The CBF_{young} map was generated from the AMBR dataset. (Bottom) Each dot (grey and red) represents an individual's Spearman's correlation between their SS map and AMBR-average CBF_{young} map. The dashed box outlines red dots, identifying outliers whose correlation values are greater than 3 scaled median absolute deviations from the median. Note that these subjects tend to show negative and weaker correlations with $CMRGlc_{young}$ (FIG. 14B) and $CMRO2_{young}$ (FIG. 14C) maps. The correlations between SS maps (FIG. 14A) and $CBF_{young}/CMRO2_{young}$ are weaker compared to those with $CMRGlc_{young}$. Also, note that the SS Youthful Index (panel **A**) and $CMRGlc_{young}$-SS maps relationships (panel **B**) start positively in younger CamCAN participants but exhibit a decline and increased variability with aging.

FIG. 15A is a graph of gray matter volume (number of voxels in (3mm)3 space) vs. SS Youthful Index. The SS Youthful Index is independent of gray matter volume, head motion, and sex differences. A group of older subjects (age > 45yrs) were selected to determine if the outliers identified (in FIG. 14A, FIG. 14B, FIG. 14C, and FIG. 14D) exhibited significant differences in their gray matter volume, head motion, or sex. Outliers (red dots in FIG. 14A, FIG. 14B, FIG. 14C, and FIG. 14D) are shown as red dots. Non-outliers (gray dots in FIG. 14A, FIG. 14B, FIG. 14C, and FIG. 14D) are shown as black dots.

FIG. 15B is a graph of head motion (mm) vs. SS Youthful Index. The SS Youthful Index is independent of gray matter volume, head motion, and sex differences. A group of older subjects (age > 45yrs) were selected to determine if the outliers identified (in FIG. 14A, FIG. 14B, FIG. 14C, and FIG. 14D) exhibited significant differences in their gray matter volume, head motion, or sex. Outliers (red dots in FIG. 14A, FIG. 14B, FIG. 14C, and FIG. 14D) are shown as red dots. Non-outliers (gray dots in FIG. 14A, FIG. 14B, FIG. 14C, and FIG. 14D) are shown as black dots.

FIG. 15C is a set of graphs of the differences in sex distributions between FIG. 15A and FIG. 15B non-outliers (top, black dots) and outliers (bottom, red dots). The SS Youthful Index is independent of gray matter volume, head

motion, and sex differences. A group of older subjects (age > 45yrs) were selected to determine if the outliers identified (in FIG. 14A, FIG. 14B, FIG. 14C, and FIG. 14D) exhibited significant differences in their gray matter volume, head motion, or sex. Outliers (red dots in FIG. 14A, FIG. 14B, FIG. 14C, and FIG. 14D) are shown as red dots. Non-outliers (gray dots in FIG. 14A, FIG. 14B, FIG. 14C, and FIG. 14D) are shown as black dots.

FIG. 16 is a conceptual framework for age-related biomarkers of neuropathology. Pathology can lead to either decreased (left) or increased (right) biomarker values. In both cases, horizontal lines indicate the median values of subjects who retain the youthful baseline. The diverging line starting from the midpoint indicates the median biomarker trajectory of subjects who significantly deviate from the youthful baseline.

FIG. 17 is a flow chart illustrating a method of identifying a brain disorder and optionally predicting a prognosis in a subject in accordance with one aspect of the disclosure.

FIG. 18 is a flow chart illustrating a method of identifying pathological neurometabolic aging in a subject in accordance with one aspect of the disclosure.

DETAILED DESCRIPTION OF THE INVENTION

The present disclosure is based, at least in part, on the discovery that power-law exponents and fractional amplitudes of low-frequency fluctuations (fALFF) in resting state functional MRI (rs-fMRI) signals offer a means of noninvasively studying the effects of glioblastoma on the whole brain and providing important prognostic information.

As shown herein, glioblastoma alters the spectral content of spontaneous whole-brain activity, which, when monitored using rs-fMRI, provides prognostic value. In particular, as compared to normal healthy whole-brain activity, suppressed low-frequency fALFF (closer to 0.01 Hz), elevated higher-frequency fALFF (closer to 0.10 Hz), and/or a relatively low power-law exponent (β) can indicate impaired brain integrity associated with glioblastoma. Thus, these metrics may serve as valuable tools for researchers to assess prognosis in

patients with glioblastomas. In some aspects, the systems and methods herein can more generally be used to assess the metabolic integrity of the brain in the setting of various other diseases and neurologic disorders including, but not limited to, brain tumors, strokes, and epilepsy. In some embodiments, the disclosed systems and methods can be used to assess the impact of systemic diseases on the brain.

One aspect of the present disclosure provides for a brain prognosis system. Another aspect of the present disclosure provides for methods of prognosis of a brain for a number of diseases, including, but not limited to, brain tumors, stroke, and epilepsy.

In some aspects, the present disclosure relates to a computer-implemented method for identifying a brain disorder in a patient. In other aspects, the computer-implemented method can select a treatment for a patient. In another aspect, the disclosed method can predict a prognosis in a brain disorder patient. In yet another aspect, the disclosed method can be used to monitor the efficacy of a treatment for a brain disorder in a patient.

A flow chart of the disclosed method 1700 of identifying a brain disorder in one embodiment is provided as FIG. 17. The method 1700 includes receiving a patient rs-fMRI dataset at 1702. An rs-fMRI dataset, as used herein, includes a plurality of time-series of brain activity fluctuations obtained from a corresponding plurality of voxels positioned throughout the brain of the patient using any of the non-invasive brain activity monitoring methods described herein. Any suitable means of measuring and quantifying fluctuations in brain activity for the voxels of the rs-fMRI dataset may be used including, but not limited to, blood-oxygen-level-dependent (BOLD) fluctuations measured using resting-state functional MRI (rs-fMRI) methods.

Referring again to FIG. 17, the method 1700 may further include transforming the time-series of the patient rs-fMRI dataset into a power spectrum density (PSD) dataset at 1704. PSD, as used herein, refers to a frequency spectrum that includes a plurality of powers of the signals of the time-series over a range of signal frequencies. PSD dataset, as used herein, refers to a dataset that includes a plurality of PSD spectra and a corresponding plurality of voxels

from the patient rs-fMRI dataset. The PSD spectra for each voxel of the PSD dataset may be generated using any suitable means including, but not limited to, Welch's averaged modified periodogram method as described in the Examples herein.

In various aspects, the PSD spectra may be generated over any suitable frequency range including, but not limited to, a lower limit of about 0.015 Hz and an upper limit of about 0.145 Hz. In other aspects, the lower limit may be 0.015 Hz, 0.016 Hz, 0.017 Hz, 0.018 Hz, 0.019 Hz, 0.020 Hz, 0.021 Hz, 0.022 Hz, 0.023 Hz, 0.024 Hz, 0.025 Hz, 0.026 Hz, 0.027 Hz, 0.028 Hz, 0.029 Hz, 0.030 Hz, 0.031 Hz, 0.032 Hz, 0.033 Hz, 0.034 Hz, 0.035 Hz, 0.036 Hz, 0.037 Hz, 0.038 Hz, 0.039 Hz, 0.040 Hz, 0.041 Hz, 0.042 Hz, 0.043 Hz, 0.044 Hz, 0.045 Hz, 0.046 Hz, 0.047 Hz, 0.048 Hz, 0.049 Hz, and 0.050 Hz. In other aspects, the upper limit may be 0.090 Hz, 0.091 Hz, 0.092 Hz, 0.093 Hz, 0.094 Hz, 0.095 Hz, 0.096 Hz, 0.097 Hz, 0.098 Hz, 0.099 Hz, 0.100 Hz, 0.101 Hz, 0.102 Hz, 0.103 Hz, 0.104 Hz, 0.105 Hz, 0.106 Hz, 0.107 Hz, 0.108 Hz, 0.109 Hz, 0.110 Hz, 0.111 Hz, 0.112 Hz, 0.113 Hz, 0.114 Hz, 0.115 Hz, 0.116 Hz, 0.117 Hz, 0.118 Hz, 0.119 Hz, 0.120 Hz, 0.121 Hz, 0.122 Hz, 0.123 Hz, 0.124 Hz, 0.125 Hz, 0.126 Hz, 0.127 Hz, 0.128 Hz, 0.129 Hz, 0.130 Hz, 0.131 Hz, 0.132 Hz, 0.133 Hz, 0.134 Hz, 0.135 Hz, 0.136 Hz, 0.137 Hz, 0.138 Hz, 0.139 Hz, 0.140 Hz, 0.141 Hz, 0.142 Hz, 0.143 Hz, 0.144 Hz, and 0.145 Hz. In one exemplary aspect, the PSD spectra may be generated over a frequency range from about 0.015 Hz to about 0.145 Hz. In another exemplary aspect, the PSD spectra may be generated over a frequency range from about 0.025 Hz to about 0.105 Hz.

Referring again to FIG. 17, the method 1700 further includes transforming the plurality of PSDs of the PSD dataset into at least one of a power law exponent dataset, a spectral slope dataset, and one or more fALFF datasets at 1706. Without being limited to any particular theory, power-law exponents and spectral slopes summarize many characteristics of a PSD in a single value. Further, fALFFs obtained at different frequency subranges of the PSDs may capture the relative prevalence of different subranges of neural activity such as slow frequency versus fast frequency activity.

In various aspects, the entire PSD dataset (i.e., all voxels) may be

transformed at 1706. In other aspects, selected portions of the PSD dataset corresponding to voxels positioned within selected brain regions may be transformed at 1706. Without being limited to any particular theory, the parameters calculated at 1706 for selected brain regions may be informative in the diagnosis and prognosis of various types of brain disorders and pathological neurometabolic aging. Non-limiting examples of selected brain regions include subcortical regions such as amygdala, hippocampus, thalamus, ventral and dorsal striatum, gray matter cortical regions such as medial and lateral parietal, prefrontal, posterior cingulate, and visual cortices, white matter, and brain stem. Additional non-limiting examples of selected brain regions include regions associated with resting-state networks (RSNs) such as default mode (DMN), visual, fronto-parietal (FP), dorsal attention (DAN), language (Lang.), salience, cinguloopercular (CO), somatomotor dorsal (SMd), somatomotor lateral (SMl), auditory, temporal pole (Tpole), medial temporal lobe (MTL), parietal medial (PMN), and parieto-occipital (PON).

In various aspects, the power law exponent dataset includes a plurality of power law exponents and corresponding voxels derived from the PSDs of the PSD dataset. In some aspects, the power law exponent is determined by fitting a power-law function to a selected frequency region of the power spectral density spectra from the PSD dataset. By way of non-limiting example, the power law exponent (also referred to herein as "β") may be calculated as the negative of the slope of a linear regression through the PSD versus frequency in a Log–Log scale. In some aspects, the selected frequency range used to determine each β may be any of the frequency ranges of the PSD spectra of the PSD database as described above. By way of non-limiting example, the selected frequency region may range from about 0.025 Hz to about 0.105 Hz.

In various other aspects, the spectral slope dataset includes a plurality of spectral slopes and corresponding voxels derived from the PSDs of the PSD dataset. In some aspects, the spectral slope is determined using a linear regression of log power against frequency within a frequency band of the PSD. In other aspects, the spectral slope is determined as the negative of the first derivative of the slope fitted to the logged power vs. frequency in its natural scale. In various aspects, the selected frequency band may be any of the

frequency ranges of the PSDs as described above. By way of non-limiting example, the selected frequency region may range from about 0.015 Hz to about 0.145 Hz.

In various other aspects, each of the at least one fALFF datasets includes a plurality of fALFFs and corresponding voxels derived from the PSDs of the PSD dataset. Without being limited to any particular theory, fALFF quantifies the relative power of each frequency of a PSD spectrum in the form of a fraction of the total spectral power of the PSD spectrum within a selected frequency band. In various aspects, the selected frequency band may be any of the frequency ranges of the PSDs as described above. In various aspects, each voxel of the fALFF includes a plurality of individual fALLFs for each frequency within the selected frequency range. By way of non-limiting example, each voxel of the fALFF may include values at 0.01 Hz intervals over a selected frequency region ranging from about 0.025 Hz to about 0.105 Hz.

In some aspects, fALFF values for each voxel within an rs-fMRI dataset are calculated at 1706 by averaging power spectral density (PSD) across runs to yield a biomarker that can be used to evaluate brain integrity as described herein.

Referring again to FIG. 17, the method 1700 includes comparing the parameter datasets produced at 1706 (power-law exponent dataset, spectral slope dataset, and/or fALFF dataset(s)) to corresponding reference datasets at 1708. In various aspects, the reference datasets include parameter datasets produced using rs-fMRI measurements obtained from a population of healthy control subjects and are representative of the characteristics of a normal healthy brain. In some aspects, the parameter datasets may be averaged over the whole brain by averaging over all voxels and the whole brain values compared. In other aspects, the parameter datasets may be averaged over one or more subregions of the brain disclosed above, and the subregion values compared.

Referring again to FIG. 17, the method includes identifying the brain disorder at 1710 based on the differences between the patient and reference parameter values produced at 1708. In some aspects, the brain disorder may be identified if the patient parameter value falls outside a range of corresponding

reference values. By way of non-limiting example, a brain disorder may be identified if the whole-brain power-law exponent of the subject falls outside of the range of reference whole-brain power-law exponents. By way of another non-limiting example, a brain disorder may be identified using a similar comparison for power-law exponents averaged over matched brain regions of the subject and reference datasets.

Referring again to FIG. 17, the method may further include predicting a prognosis of the subject with the brain disorder at 1712 in various additional aspects. In one aspect, the prognosis may be determined based on fALFF values at the lowest and highest frequency ranges of the PSD spectra. By way of non-limiting example, the fALFF values within a lowest frequency range of about 0.025 Hz to about 0.045 Hz and/or within a highest frequency range of about 0.085 Hz to about 0.105 Hz may be used to predict a prognosis. By way of non-limiting example, the subject's prognosis may be predicted based on a Kaplan-Meier survival curve based on cortical gray matter fALFF evaluated in the same lowest and highest frequency bands from a population of subjects with brain disorder.

In various aspects, the disclosed systems and methods are used to determine an additional metric used to quantify pathological neurometabolic aging in a patient, the SS Youthful Index, based on the fractional amplitudes of low-frequency fluctuations (fALFFs) of an individual/patient. The SS Youthful Index quantifies the neurometabolic aging process within different cortical regions of the brain, providing for the use of accessible whole-brain imaging to monitor and understand brain aging and health. In some aspects, the spectral properties of rs-fMRI BOLD signals are used to identify various aspects of the neurometabolic aging process.

The disclosed SS Youthful Index may be used in a method of identifying pathological neurometabolic aging in a patient. A flow chart of the disclosed method 1800 of identifying a brain disorder in one embodiment is provided as FIG. 18. The method 1800 includes receiving a patient rs-fMRI dataset at 1802. An rs-fMRI dataset, as used herein, includes a plurality of time-series of brain activity fluctuations obtained from a corresponding plurality of voxels positioned

throughout the brain of the patient using any of the non-invasive brain activity monitoring methods described herein. Any suitable means of measuring and quantifying fluctuations in brain activity for the voxels of the rs-fMRI dataset may be used including, but not limited to, blood-oxygen-level-dependent (BOLD) fluctuations measured using resting-state functional MRI (rs-fMRI) methods.

Referring again to FIG. 18, the method 1800 may further include transforming the time-series of the patient rs-fMRI dataset into a power spectrum density (PSD) dataset at 1804. PSD, as used herein, refers to a frequency spectrum that includes a plurality of powers of the signals of the time-series over a range of signal frequencies. PSD dataset, as used herein, refers to a dataset that includes a plurality of PSD spectra and a corresponding plurality of voxels from the patient rs-fMRI dataset. The PSD spectra for each voxel of the PSD dataset may be generated using any suitable means including, but not limited to, Welch's averaged modified periodogram method as described in the Examples herein.

In various aspects, the PSD spectra may be generated over any suitable frequency range including, but not limited to, a lower limit of about 0.015 Hz and an upper limit of about 0.145 Hz. In other aspects, the lower limit may be 0.015 Hz, 0.016 Hz, 0.017 Hz, 0.018 Hz, 0.019 Hz, 0.020 Hz, 0.021 Hz, 0.022 Hz, 0.023 Hz, 0.024 Hz, 0.025 Hz, 0.026 Hz, 0.027 Hz, 0.028 Hz, 0.029 Hz, 0.030 Hz, 0.031 Hz, 0.032 Hz, 0.033 Hz, 0.034 Hz, 0.035 Hz, 0.036 Hz, 0.037 Hz, 0.038 Hz, 0.039 Hz, 0.040 Hz, 0.041 Hz, 0.042 Hz, 0.043 Hz, 0.044 Hz, 0.045 Hz, 0.046 Hz, 0.047 Hz, 0.048 Hz, 0.049 Hz, and 0.050 Hz. In other aspects, the upper limit may be 0.090 Hz, 0.091 Hz, 0.092 Hz, 0.093 Hz, 0.094 Hz, 0.095 Hz, 0.096 Hz, 0.097 Hz, 0.098 Hz, 0.099 Hz, 0.100 Hz, 0.101 Hz, 0.102 Hz, 0.103 Hz, 0.104 Hz, 0.105 Hz, 0.106 Hz, 0.107 Hz, 0.108 Hz, 0.109 Hz, 0.110 Hz, 0.111 Hz, 0.112 Hz, 0.113 Hz, 0.114 Hz, 0.115 Hz, 0.116 Hz, 0.117 Hz, 0.118 Hz, 0.119 Hz, 0.120 Hz, 0.121 Hz, 0.122 Hz, 0.123 Hz, 0.124 Hz, 0.125 Hz, 0.126 Hz, 0.127 Hz, 0.128 Hz, 0.129 Hz, 0.130 Hz, 0.131 Hz, 0.132 Hz, 0.133 Hz, 0.134 Hz, 0.135 Hz, 0.136 Hz, 0.137 Hz, 0.138 Hz, 0.139 Hz, 0.140 Hz, 0.141 Hz, 0.142 Hz, 0.143 Hz, 0.144 Hz, and 0.145 Hz. In one exemplary aspect, the PSD spectra may be generated over a frequency range from about 0.015 Hz to about 0.145 Hz. In another exemplary aspect, the PSD spectra may

be generated over a frequency range from about 0.025 Hz to about 0.105 Hz.

Referring again to FIG. 18, the method 1800 further includes transforming the plurality of PSDs of the PSD dataset into a spectral slope dataset at 1806.

In various aspects, the entire PSD dataset (i.e., all voxels) may be transformed at 1806. In other aspects, selected portions of the PSD dataset corresponding to voxels positioned within selected brain regions may be transformed at 1806. Without being limited to any particular theory, the parameters calculated at 1806 for selected brain regions may be informative in the diagnosis and prognosis of various types of brain disorders and pathological neurometabolic aging. Non-limiting examples of selected brain regions include subcortical regions such as amygdala, hippocampus, thalamus, ventral and dorsal striatum, gray matter cortical regions such as medial and lateral parietal, prefrontal, posterior cingulate, and visual cortices, white matter, and brain stem. Additional non-limiting examples of selected brain regions include regions associated with resting-state networks (RSNs) such as default mode (DMN), visual, fronto-parietal (FP), dorsal attention (DAN), language (Lang.), salience, cinguloopercular (CO), somatomotor dorsal (SMd), somatomotor lateral (SMl), auditory, temporal pole (Tpole), medial temporal lobe (MTL), parietal medial (PMN), and parieto-occipital (PON).

In various aspects, the power law exponent dataset includes a plurality of power law exponents and corresponding voxels derived from the PSDs of the PSD dataset. In some aspects, the power law exponent is determined by fitting a power-law function to a selected frequency region of the power spectral density spectra from the PSD dataset. By way of non-limiting example, the power law exponent (also referred to herein as “β”) may be calculated as the negative of the slope of a linear regression through the PSD versus frequency in a Log–Log scale. In some aspects, the selected frequency range used to determine each β may be any of the frequency ranges of the PSD spectra of the PSD database as described above. By way of non-limiting example, the selected frequency region may range from about 0.025 Hz to about 0.105 Hz.

In various other aspects, the spectral slope dataset includes a plurality of spectral slopes and corresponding voxels derived from the PSDs of the PSD

dataset. In some aspects, the spectral slope is determined using a linear regression of log power against frequency within a frequency band of the PSD. In other aspects, the spectral slope is determined as the negative of the first derivative of the slope fitted to the logged power vs. frequency in its natural scale. In various aspects, the selected frequency band may be any of the frequency ranges of the PSDs as described above. By way of non-limiting example, the selected frequency region may range from about 0.015 Hz to about 0.145 Hz.

Referring again to FIG. 18, the method 1800 includes comparing the patient spectral slope datasets produced at 1806 to a corresponding reference spectral slope dataset at 1808. In various aspects, the reference spectral slope dataset includes spectral slope datasets produced using rs-fMRI measurements obtained from a population of healthy control subjects and are representative of the characteristics of a normal healthy brain. In some aspects, the patient and reference spectral slope datasets may be averaged over the whole brain by averaging over all voxels and the whole brain values compared. In other aspects, the patient and reference spectral slope datasets may be averaged over one or more subregions of the brain disclosed above, and the subregion values compared.

Referring again to FIG. 18, the method 1800 may further include transforming the comparison of the patient and reference spectral slope datasets into an SS Youthful Index at 1810. In various aspects, the SS Youthful Index is calculated by obtaining a Spearman correlation between the patient SS dataset and the reference SS dataset. In some aspects, the SS Youthful Index may be based on a Spearman correlation of the entire patient and reference SS datasets. In other aspects, the SS Youthful Index may be based on a Spearman correlation of a selected portion of the patient and reference SS datasets. In various aspects, the selected portion of the SS datasets may be selected PSD frequency ranges, selected brain regions, brain structures, brain tissue types, or resting state functional networks. Non-limiting examples of these selected portions are described in detail above.

Although the calculation of the SS Youthful Index is disclosed herein in

terms of spectral slope (SS) datasets, any spectral measure of neurological function may be used in a similar manner using other measures of neurological function disclosed herein including, but not limited to, power-law coefficient β, fALFFs over one or more selected PSD frequency ranges, and any other suitable measure of neurological activity within limitation.

In various aspects, the SS Youthful Index may be derived from spectral measurements obtained over the full brain or selected portions of the brain structures, brain tissue types, or brain resting state functional networks. In one on-limiting example, the SS Youthful Index is derived from PSD datasets obtained from the cortical grey matter of the patient and reference healthy population.

Referring again to FIG. 18, the method 1800 may further include predicting pathological neurometabolic aging in the patient based on the SS Youthful Index at 1812. In various aspects, pathological neurometabolic aging is predicted if the patient SS Youthful Index value falls outside of a threshold range representative of the SS Youthful Indices of normal, healthy subjects. In some aspects, the threshold range includes a range defied by the scaled median absolute deviations from the median SS Youthful Indices of a population of normal, healthy subjects. In various aspects, the threshold range may be 0.5 scaled median absolute deviations, one scaled median absolute deviation, two scaled median absolute deviations, three scaled median absolute deviations, or four scaled median absolute deviations from the median SS Youthful Indices of a population of normal, healthy subjects. In one exemplary aspect, the threshold range is three scaled median absolute deviations from the median SS Youthful Indices of a population of normal, healthy subjects.

As described in the Examples below, brain-wide spectral properties in a group of patients with glioblastoma (N=189) and an age-matched group of reference participants (N = 189) were evaluated, and power-law exponents and fALFFs were estimated for each patient/participant and compared. Glioblastomas induced brain-wide shifts in both power-law exponent and fALFF; these metrics also correlated with metabolically relevant epigenetic features and comorbid conditions. Changes in brain-wide spectral properties were also

strongly associated with overall survival in glioblastoma patients.

The disclosed systems and methods provide a foundation for non-invasive radiomic biomarkers that can improve glioblastoma diagnosis, prognosis, and treatment. The disclosed systems and methods further provide insight into the management and treatment of glioblastoma, which has a major impact on clinical decision-making and trial design for patients with glioblastomas. Enhancing the understanding and care of these patients – who typically have a mean survival of just fourteen months - is an urgent need that the systems and methods of the current disclosure address.

In various aspects, at least a portion of the methods disclosed herein may be implemented using various computing systems and devices as described below. FIG. 1 depicts a simplified block diagram of a computing device 300 for implementing the system and methods described herein.

As illustrated in FIG. 1, the computer system 300 may include a computing device 302. In one aspect, the computing device 302 is part of a server system 304, which also includes a database server 306. The computing device 302 is in communication with a database 308 through the database server 306. The computing device 302 is communicably coupled to a user-computing device 330 through a network 350.

The network 350 may be any network that allows local area or wide area communication between the devices. For example, the network 350 may allow communicative coupling to the Internet through at least one of many interfaces including, but not limited to, at least one of a network, such as the Internet, a local area network (LAN), a wide area network (WAN), an integrated services digital network (ISDN), a dial-up-connection, a digital subscriber line (DSL), a cellular phone connection, and a cable modem.

The user-computing device 330 may be any device capable of accessing the Internet including, but not limited to, a desktop computer, a laptop computer, a personal digital assistant (PDA), a cellular phone, a smartphone, a tablet, a phablet, wearable electronics, smartwatch, or other web-based connectable equipment or mobile devices.

In other aspects, the computing device 302 is configured to perform a

plurality of tasks associated with the production of a brain prognosis and method of selecting a treatment for a brain disorder using the brain prognosis system as described herein. The computing device 300 may be configured to implement at least a portion of the tasks associated with the disclosed methods of identifying brain disorders in a patient, estimating a prognosis of a patient with a brain disorder, and/or identifying pathological neurometabolic aging in a patient. In various aspects, the resulting diagnoses and estimated prognoses are determined based on the analysis of brain activity within various regions of the patient's brain. In various aspects, the brain activity is monitored using any suitable method of brain activity measurement, including, but not limited to, functional magnetic resonance imaging (fMRI), near-infrared spectroscopy (NIRS), magnetoencephalography (MEG), electroencephalography (EEG), and any other suitable method of brain activity measurement without limitation. In an exemplary embodiment, the medical imaging data can be blood oxygenation level-dependent (BOLD) MRI data. In some embodiments, the medical imaging data can be BOLD resting state fMRI obtained from a patient in an inactive, non-stimulated state. In some aspects, the user computing device 330 may be communicably coupled to a system or device configured to monitor the brain activity of the patient including, but not limited to, an MRI scanner 334, as illustrated in FIG. 1.

FIG. 2 depicts a component configuration 400 of computing device 402, which includes database 410 along with other related computing components. In some aspects, computing device 402 is similar to computing device 302 (shown in FIG. 1). A user 404 may access components of computing device 402. In some aspects, database 410 is similar to database 308 (shown in FIG. 1).

In one aspect, database 410 includes patient rs-fMRI data 418, reference rs-fMRI data 422, rs-fMRI analysis data 420, and diagnosis/prognosis data 424. In various aspects, patient rs-fMRI data 418 and reference rs-fMRI data 422 include rs-fMRI datasets obtained from a patient's brain and the brains of healthy normal subjects, respectively. In some aspects, the reference rs-fMRI data 422 may further contain rs-fMRI datasets obtained from the brains of patients with one or more brain disorders. Each rs-fMRI dataset includes a plurality of brain activity measurements for a corresponding plurality of voxels at various positions

within the brain of one subject. The rs-fMRI datasets may be obtained using any suitable brain activity monitoring method as described above including, but not limited to BOLD rs-fMRI.

In various aspects, the rs-fMRI analysis data 420 includes equations and constants used to implement the calculation of the various parameters used to identify a brain disorder in a patient, predict the prognosis of a patient with a brain disorder, and/or identify pathological neurometabolic aging in a patient as described herein. In various aspects, the rs-fMRI analysis data 420 further includes the calculated values of parameters characterizing the brain activity patterns of the patient-derived from analysis of the patient rs-fMRI data 418 as described herein including, but not limited to fALFFs at one or more frequency ranges, power law exponents (β), and SS Youthful Indices, as described herein.

In various aspects, the diagnosis/prognosis data 424 may include various diagnostic ranges, limits, or threshold values used to determine or estimate the occurrence of a brain disorder, a prognosis related to a brain disorder, and/or the occurrence of pathological neurometabolic aging based on the various characterizing parameters based on the various values from the rs-fMRI analysis data 420.

Computing device 402 also includes a number of components that perform specific tasks related to the computations used to implement the various methods described herein. In some aspects, shown in FIG. 2, the computing device 402 includes a data storage device 430, a power law exponent component 440, an fALFF analysis component 450, a communication component 460, and an SS Youthful Index Component. Data storage device 430 is configured to store data received or generated by computing device 402, such as any of the data stored in database 410 or any outputs of processes implemented by any component of computing device 402. The power law exponent component 440 is configured to produce an analysis of the spectra of the brain activity data for at least a portion of the voxels of the rs-fMRI datasets from the reference rs-fMRI data 422 and patient rs-fMRI data 418 data to produce a corresponding plurality of spectral slopes or power law exponents as described herein. In other aspects, the power law exponent component 440 may

produce a spectral slope (SS) dataset map that includes a plurality of the spectral slopes and associated voxels from an rs-fMRI dataset as disclosed herein In some aspects, the power law exponent component 440 may further assemble a spectral slope (SS) map that includes a plurality of the spectral slopes mapped to the positions of the voxels from a rs-fMRI dataset as disclosed herein.

The fALFF analysis component 450 is configured to produce an analysis of the spectra of the brain activity data for at least a portion of the voxels of the rs-fMRI datasets from the reference rs-fMRI data 422 and/or patient rs-fMRI data 418 data to produce corresponding fALFF values as described herein. In some aspects, the fALFF analysis component 450 is configured to produce fALFF values for a selected set of frequency ranges of the spectra of the brain activity data including, but not limited to, low-frequency fALLF (~0.01 Hz) and high-frequency fALFF (~0.1 Hz) as described herein.

In various aspects, the SS Youthful Index component 470 is configured to produce an SS Youthful Index based on differences between an SS dataset produced from an rs-fMRI dataset of a patient and the corresponding reference SS dataset produced from a healthy subject as described herein.

The communication component 460 is configured to enable communications between computing device 402 and other devices (e.g. user computing device 330 and sequencing system 310, shown in FIG. 1) over a network, such as a network 350 (shown in FIG. 1), or a plurality of network connections using predefined network protocols such as TCP/IP (Transmission Control Protocol/Internet Protocol).

FIG. 3 depicts a configuration of a remote or user-computing device 502, such as user-computing device 330 (shown in FIG. 1). Computing device 502 may include a processor 505 for executing instructions. In some aspects, executable instructions may be stored in a memory area 510. Processor 505 may include one or more processing units (e.g., in a multi-core configuration). Memory area 510 may be any device allowing information such as executable instructions and/or other data to be stored and retrieved. Memory area 510 may include one or more computer-readable media.

Computing device 502 may also include at least one media output component 515 for presenting information to a user 501. Media output component 515 may be any component capable of conveying information to user 501. In some aspects, media output component 515 may include an output adapter, such as a video adapter and/or an audio adapter. An output adapter may be operatively coupled to processor 505 and operatively coupleable to an output device such as a display device (e.g., a liquid crystal display (LCD), organic light emitting diode (OLED) display, cathode ray tube (CRT), or "electronic ink" display) or an audio output device (e.g., a speaker or headphones). In some aspects, media output component 515 may be configured to present an interactive user interface (e.g., a web browser or client application) to user 501.

In some aspects, computing device 502 may include an input device 520 for receiving input from user 501. Input device 520 may include, for example, a keyboard, a pointing device, a mouse, a stylus, a touch-sensitive panel (e.g., a touchpad or a touch screen), a camera, a gyroscope, an accelerometer, a position detector, and/or an audio input device. A single component such as a touch screen may function as both an output device of media output component 515 and input device 520.

Computing device 502 may also include a communication interface 525, which may be communicatively coupleable to a remote device. Communication interface 525 may include, for example, a wired or wireless network adapter or a wireless data transceiver for use with a mobile phone network (e.g., Global System for Mobile communications (GSM), 3G, 4G, or Bluetooth) or other mobile data network (e.g., Worldwide Interoperability for Microwave Access (WIMAX)).

Stored in memory area 510 are, for example, computer-readable instructions for providing a user interface to user 501 via media output component 515 and, optionally, receiving and processing input from input device 520. A user interface may include, among other possibilities, a web browser and client application. Web browsers enable users 501 to display and interact with media and other information typically embedded on a web page or a website from a web server. A client application allows users 501 to interact with a server

application associated with, for example, a vendor or business.

FIG. 4 illustrates an example configuration of a server system 602. Server system 602 may include, but is not limited to, database server 306 and computing device 302 (both shown in FIG. 1). In some aspects, server system 602 is similar to server system 304 (shown in FIG. 1). Server system 602 may include a processor 605 for executing instructions. Instructions may be stored in a memory area 625, for example. Processor 605 may include one or more processing units (e.g., in a multi-core configuration).

Processor 605 may be operatively coupled to a communication interface 615 such that server system 602 may be capable of communicating with a remote device such as user computing device 330 (shown in FIG. 1) or another server system 602. For example, communication interface 615 may receive requests from user computing device 330 via network 350 (shown in FIG. 1).

Processor 605 may also be operatively coupled to a storage device 625. Storage device 625 may be any computer-operated hardware suitable for storing and/or retrieving data. In some aspects, storage device 625 may be integrated into server system 602. For example, server system 602 may include one or more hard disk drives as storage device 625. In other aspects, storage device 625 may be external to server system 602 and may be accessed by a plurality of server systems 602. For example, storage device 625 may include multiple storage units such as hard disks or solid-state disks in a redundant array of inexpensive disks (RAID) configuration. Storage device 625 may include a storage area network (SAN) and/or a network attached storage (NAS) system.

In some aspects, processor 605 may be operatively coupled to storage device 625 via a storage interface 620. Storage interface 620 may be any component capable of providing processor 605 with access to storage device 625. Storage interface 620 may include, for example, an Advanced Technology Attachment (ATA) adapter, a Serial ATA (SATA) adapter, a Small Computer System Interface (SCSI) adapter, a RAID controller, a SAN adapter, a network adapter, and/or any component providing processor 605 with access to storage device 625.

Memory areas 510 (shown in FIG. 3) and 610 may include but are not

limited to, random access memory (RAM) such as dynamic RAM (DRAM) or static RAM (SRAM), read-only memory (ROM), erasable programmable read-only memory (EPROM), electrically erasable programmable read-only memory (EEPROM), and non-volatile RAM (NVRAM). The above memory types are examples only and are thus not limiting as to the types of memory usable for storage of a computer program.

The computer systems and computer-implemented methods discussed herein may include additional, less, or alternate actions and/or functionalities, including those discussed elsewhere herein. The computer systems may include or be implemented via computer-executable instructions stored on non-transitory computer-readable media. The methods may be implemented via one or more local or remote processors, transceivers, servers, and/or sensors (such as processors, transceivers, servers, and/or sensors mounted on vehicle or mobile devices, or associated with smart infrastructure or remote servers), and/or via computer-executable instructions stored on non-transitory computer-readable media or medium.

In some aspects, a computing device is configured to implement machine learning, such that the computing device "learns" to analyze, organize, and/or process data without being explicitly programmed. Machine learning may be implemented through machine learning (ML) methods and algorithms. In one aspect, a machine learning (ML) module is configured to implement ML methods and algorithms. In some aspects, ML methods and algorithms are applied to data inputs and generate machine learning (ML) outputs. Data inputs may further include sequencing data, sensor data, image data, video data, telematics data, authentication data, authorization data, security data, mobile device data, geolocation information, transaction data, personal identification data, financial data, usage data, weather pattern data, "big data" sets, and/or user preference data. In some aspects, data inputs may include certain ML outputs.

In some aspects, at least one of a plurality of ML methods and algorithms may be applied, which may include but are not limited to linear or logistic regression, instance-based algorithms, regularization algorithms, decision trees, Bayesian networks, cluster analysis, association rule learning, artificial neural

networks, deep learning, dimensionality reduction, and support vector machines. In various aspects, the implemented ML methods and algorithms are directed toward at least one of a plurality of categorizations of machine learning, such as supervised learning, unsupervised learning, and reinforcement learning.

In one aspect, ML methods and algorithms are directed toward supervised learning, which involves identifying patterns in existing data to make predictions about subsequently received data. Specifically, ML methods and algorithms directed toward supervised learning are "trained" through training data, which includes example inputs and associated example outputs. Based on the training data, the ML methods and algorithms may generate a predictive function that maps outputs to inputs and utilize the predictive function to generate ML outputs based on data inputs. The example inputs and example outputs of the training data may include any of the data inputs or ML outputs described above.

In another aspect, ML methods and algorithms are directed toward unsupervised learning, which involves finding meaningful relationships in unorganized data. Unlike supervised learning, unsupervised learning does not involve user-initiated training based on example inputs with associated outputs. Rather, in unsupervised learning, unlabeled data, which may be any combination of data inputs and/or ML outputs as described above, is organized according to an algorithm-determined relationship.

In yet another aspect, ML methods and algorithms are directed toward reinforcement learning, which involves optimizing outputs based on feedback from a reward signal. Specifically ML methods and algorithms directed toward reinforcement learning may receive a user-defined reward signal definition, receive a data input, utilize a decision-making model to generate an ML output based on the data input, receive a reward signal based on the reward signal definition and the ML output, and alter the decision-making model so as to receive a stronger reward signal for subsequently generated ML outputs. The reward signal definition may be based on any of the data inputs or ML outputs described above. In one aspect, an ML module implements reinforcement learning in a user recommendation application. The ML module may utilize a

decision-making model to generate a ranked list of options based on user information received from the user and may further receive selection data based on a user selection of one of the ranked options. A reward signal may be generated based on comparing the selection data to the ranking of the selected option. The ML module may update the decision-making model such that subsequently generated rankings more accurately predict a user selection.

The methods and algorithms of the invention may be enclosed in a controller or processor. Furthermore, methods and algorithms of the present invention can be embodied as a computer-implemented method or methods for performing such computer-implemented method or methods, and can also be embodied in the form of a tangible or non-transitory computer-readable storage medium containing a computer program or other machine-readable instructions (herein “computer program”), wherein when the computer program is loaded into a computer or other processor (herein “computer”) and/or is executed by the computer, the computer becomes an apparatus for practicing the method or methods. Storage media for containing such computer programs include, for example, floppy disks and diskettes, compact disk (CD)-ROMs (whether or not writeable), DVD digital disks, RAM and ROM memories, computer hard drives and back-up drives, external hard drives, “thumb” drives, and any other storage medium readable by a computer. The method or methods can also be embodied in the form of a computer program, for example, whether stored in a storage medium or transmitted over a transmission medium such as electrical conductors, fiber optics or other light conductors, or by electromagnetic radiation, wherein when the computer program is loaded into a computer and/or is executed by the computer, the computer becomes an apparatus for practicing the method or methods. The method or methods may be implemented on a general-purpose microprocessor or on a digital processor specifically configured to practice the process or processes. When a general-purpose microprocessor is employed, the computer program code configures the circuitry of the microprocessor to create specific logic circuit arrangements. Storage medium readable by a computer includes medium being readable by a computer per se or by another machine that reads the computer instructions for providing those instructions to a computer for controlling its operation. Such machines may

include, for example, machines for reading the storage media mentioned above.

A control sample or a reference sample as described herein can be a sample from a healthy subject. A reference value can be used in place of a control or reference sample, which was previously obtained from a healthy subject or a group of healthy subjects. A control sample or a reference sample can also be a sample with a known amount of a detectable compound or a spiked sample.

Definitions and methods described herein are provided to better define the present disclosure and to guide those of ordinary skill in the art in the practice of the present disclosure. Unless otherwise noted, terms are to be understood according to conventional usage by those of ordinary skill in the relevant art.

In some embodiments, numbers expressing quantities of ingredients, properties such as molecular weight, reaction conditions, and so forth, used to describe and claim certain embodiments of the present disclosure are to be understood as being modified in some instances by the term “about.” In some embodiments, the term “about” is used to indicate that a value includes the standard deviation of the mean for the device or method being employed to determine the value. In some embodiments, the numerical parameters set forth in the written description and attached claims are approximations that can vary depending upon the desired properties sought to be obtained by a particular embodiment. In some embodiments, the numerical parameters should be construed in light of the number of reported significant digits and by applying ordinary rounding techniques. Notwithstanding that the numerical ranges and parameters setting forth the broad scope of some embodiments of the present disclosure are approximations, the numerical values set forth in the specific examples are reported as precisely as practicable. The numerical values presented in some embodiments of the present disclosure may contain certain errors necessarily resulting from the standard deviation found in their respective testing measurements. The recitation of ranges of values herein is merely intended to serve as a shorthand method of referring individually to each separate value falling within the range. Unless otherwise indicated herein, each

individual value is incorporated into the specification as if it were individually recited herein. The recitation of discrete values is understood to include ranges between each value.

In some embodiments, the terms “a” and “an” and “the” and similar references used in the context of describing a particular embodiment (especially in the context of certain of the following claims) can be construed to cover both the singular and the plural, unless specifically noted otherwise. In some embodiments, the term “or” as used herein, including the claims, is used to mean “and/or” unless explicitly indicated to refer to alternatives only or the alternatives are mutually exclusive.

The terms “comprise,” “have” and “include” are open-ended linking verbs. Any forms or tenses of one or more of these verbs, such as “comprises,” “comprising,” “has,” “having,” “includes” and “including,” are also open-ended. For example, any method that “comprises,” “has” or “includes” one or more steps is not limited to possessing only those one or more steps and can also cover other unlisted steps. Similarly, any composition or device that “comprises,” “has” or “includes” one or more features is not limited to possessing only those one or more features and can cover other unlisted features.

All methods described herein can be performed in any suitable order unless otherwise indicated herein or otherwise clearly contradicted by context. The use of any and all examples, or exemplary language (e.g., “such as”) provided with respect to certain embodiments herein is intended merely to better illuminate the present disclosure and does not pose a limitation on the scope of the present disclosure otherwise claimed. No language in the specification should be construed as indicating any non-claimed element essential to the practice of the present disclosure.

Groupings of alternative elements or embodiments of the present disclosure disclosed herein are not to be construed as limitations. Each group member can be referred to and claimed individually or in any combination with other members of the group or other elements found herein. One or more members of a group can be included in, or deleted from, a group for reasons of convenience or patentability. When any such inclusion or deletion occurs, the

specification is herein deemed to contain the group as modified thus fulfilling the written description of all Markush groups used in the appended claims.

All publications, patents, patent applications, and other references cited in this application are incorporated herein by reference in their entirety for all purposes to the same extent as if each individual publication, patent, patent application, or other reference was specifically and individually indicated to be incorporated by reference in its entirety for all purposes. Citation of a reference herein shall not be construed as an admission that such is prior art to the present disclosure.

Having described the present disclosure in detail, it will be apparent that modifications, variations, and equivalent embodiments are possible without departing from the scope of the present disclosure defined in the appended claims. Furthermore, it should be appreciated that all examples in the present disclosure are provided as non-limiting examples.

EXAMPLES

The following non-limiting examples are provided to further illustrate the present disclosure.

EXAMPLE 1 - GLIOBLASTOMAS ALTER THE SPECTRAL CONTENT OF SPONTANEOUS WHOLE-BRAIN ACTIVITY

Glioblastomas, a highly aggressive form of brain cancer, are a brain-wide disease.

To characterize the impact of tumor burden on whole-brain resting-state functional magnetic resonance imaging (rs-fMRI) activity, the following experiments were conducted. rs-fMRI signals were analyzed in the temporal frequency domain in terms of the power-law exponent and fractional amplitude of low-frequency fluctuations (fALFF). 189 patients with glioblastoma were contrasted against 189 age-matched healthy subject participants from a reference OASIS dataset. The patient and reference OASIS datasets were matched for age and head motion. The principal finding was markedly flatter spectra and reduced grey matter fALFF in the patients as compared to the reference OASIS dataset. It is posited that the whole-brain spectral change is

attributable to the global dysregulation of excitatory and inhibitory balance in the tumor-bearing brain. Additionally, it was observed that clinical comorbidities, in particular, seizures, and MGMT promoter methylation, were associated with flatter spectra. Notably, the degree of change in spectra was predictive of overall survival. The findings suggest that frequency domain analysis of rs-fMRI offers a means of noninvasively studying the effects of glioblastoma on the whole brain while providing important prognostic information.

Participant demographics were obtained, such as clinical characteristics including the extent of resection, tumor volume, Karnofsky Performance Status (KPS), MGMT methylation status, EGFR amplification status, TERT mutation status, and PTEN mutation status, as tabulated in Table 1 below. Survival time was calculated as the difference between the patient's first clinical visit and the date of death. Comorbidities included in the analysis are stroke and seizure (either had a history of or presented with); history of deep vein thrombosis (DVT) or pulmonary embolism (PE); chronic kidney disease (CKD); diabetes; hypertension; tobacco use; hyperlipidemia; and BMI > 30.

189 patients with glioblastoma (Age = 61.1 ± 11.3; M:F ratio = 119:80) and 189 reference subjects (Age = 68.0 ± 10.8 M:F ratio = 80:109) were included in this study. Head movement during scanning was used as an index of fMRI data quality and was matched across the two groups. Glioblastomas were segmented on the basis of contrast-enhanced T1w and FLAIR images. FIG. 5C shows a tumor distribution heatmap compiled in the patient group. Tumor volume, the extent of resection, genetic status (MGMT, EGFR, PTEN, and TERT), Karnofsky Performance Scale (KPS), and the follow-up administration of Stupp protocol post-surgery are summarized in Table 1.

Table 1. Clinical characteristics of glioblastoma patients.

CE volume (cm^3)	42.5 ± 34.2	
FLAIR volume (cm^3)	119.0 ± 67.8	
Extent of resection	GTR = 60 NTR = 28 STR = 47	Biopsy = 3 LITT = 4 Missing = 4 None = 43

MGMT promoter methylation	Methylated = 69 Non-methylated = 113 Missing = 7
EGFR amplification	Positive = 69 Negative = 108 Missing = 12
PTEN mutation	Mutant = 97 Wildtype = 78 Missing = 14
TERT promoter mutation	Mutant = 48 Wildtype = 116 Missing = 25
KPS	< 70 = 27 ≥ 70 = 154 Missing = 8
Stupp Protocol	Received Stupp protocol = 121 Radiotherapy, no chemo = 39 None = 18 Missing = 11

CE = contrast-enhanced; FLAIR = fluid attenuated inversion recovery; GTR = gross total resection; NTR = near total resection; STR = sub-total resection; LITT = laser interstitial thermal therapy; KPS = Karnofsky performance score

The reference dataset comprised 189 individuals obtained from the OASIS3 dataset, which includes 1098 participants. For this work, we included participants that met the following inclusion criteria: Clinical Dementia Rating (CDR) score of zero at every assessment session, MRI acquired with Siemens TIM Trio 3T scanner; the presence of at least two rs-fMRI runs plus T1-weighted (T1w) and T2-weighted (T2w) structural images used for anatomic registration; participants with root mean square head motion (in mm) as determined by the realignment procedure < 1.15 mm. Of all the participants that met the inclusion criteria, we selected 189 individuals to statistically match the head motion profile to the patient group. The resting state fMRI data included two 6-minute runs (328 frames) acquired while participants were asked to remain still with their eyes open (voxel size $(3mm)^3$ isotropic; echo time = 27 ms; repetition time = 2.2 or 2.5s).

The clinical dataset comprised 189 glioblastoma patients aged 21 – 86 (average 61 years), which was retrospectively identified in a neurosurgery brain

tumor database. Inclusion criteria included: a new diagnosis of primary glioblastoma; age above 18 years; MRI at WUSM including fMRI for pre-surgical planning; adequate tumor segmentation; IDH1 wild-type; and root mean square head motion < 1.15 mm. Exclusion criteria included: prior brain surgery and inability to have an MRI scan. All analyses were conducted retrospectively using preoperative data.

Patients were scanned with either a 3T Trio or Skyra scanner (Siemens, Erlangen, Germany) using a standard clinical pre-surgical tumor protocol. Anatomical imaging included a T1w magnetization prepared rapid acquisition (MP-RAGE) and a T2w fast spin echo, both with a voxel size of $(1mm)^3$, and a FLAIR image used for tumor segmentation. rs-fMRI was acquired using a BOLD-sensitized EPI sequence (voxel size $(3mm)^3$ isotropic; echo time = 27 ms; repetition time = 2.2 – 2.9s; field of view = 256mm; flip angle = 90°). Two rs-fMRI runs were obtained in each patient (320 frames); each run included 160 frames.

Initial fMRI preprocessing followed conventional practice. Briefly, this included compensation for slice-dependent time shifts, elimination of systematic odd-even slice intensity differences due to the interleaved acquisition, and rigid body correction of head movement within and across runs. The preprocessed fMRI data were then resampled in register with the structural data in $(3mm)^3$ atlas space using a composition of the initial affine transform and a warping map (computed using the ANTs registration with cost function masking) connecting the fMRI volumes with the T1w structural image. Motion correction was included in the final resampling to generate a volumetric time series in $(3mm)^3$ atlas space. Additional preprocessing included voxel-wise removal of linear trends over each fMRI run, temporal low-pass filtering retaining frequencies below 0.15Hz, and regression of nuisance waveforms. Regressors were derived from the 6 head motion time series, time series extracted from regions in CSF, and the signal evaluated over the whole brain. Finally, spatial smoothing was applied (6mm full width at half maximum (FWHM) Gaussian blur in each direction).

To minimize the impact of subject head motion at both the individual-level analysis and group-level comparison, we evaluated root mean square (RMS) head motion (in mm) as determined by the realignment procedure. The exclusion threshold of head motion was determined as an RMS head motion value greater

than 3 scaled median absolute deviation (MAD) from the median of RMS head motion values evaluated over all patients. Participants with RMS head motion > 1.15 mm were excluded from reference and patient groups. The finally obtained head motion distributions were comparable across the reference and patient groups.

The time series extracted from each voxel was transformed to the frequency domain using Welch's averaged modified periodogram method (*pwelch* function in Matlab). Each run consists of 164 and 160 frames for the reference and patient datasets, respectively. The first three frames were ignored to allow for steady-state magnetization. A rectangular window of 75 frames with a 50% overlap between segments was used to compute the power spectral density (PSD) estimate in each run and power spectra were averaged across runs. Since the lowest detectable frequency is determined by the window size (75 samples), the lowest detectable frequencies are different across patients (0.023 – 0.03 Hz) based on varying sampling rates (TR = 2.2s – 2.9s; SR = 0.345 – 0.455 Hz). Accordingly, we obtained the power spectra within the frequency range (0.025 – 0.105 Hz) for subsequent analyses.

Fractional ALFF (fALFF) at each frequency (0.025 to 0.10 5Hz at a 0.01 Hz interval) was computed as the ratio of the power of the specific frequency to that of the frequency range, 0.03 – 0.15Hz. Power-law scaling behavior is indicative of scale invariance: if $P(f) \propto 1/f^{\beta}$, then the ratio of P measured at two different frequencies, f_1 and f_2, depends on the ratio of the two defined frequencies. Several studies have shown that fMRI signal exhibits a scale-free activity similar to that seen in electrophysiologic and cellular studies, such as local field potentials (LFP), electroencephalography (EEG), action potential rates, and the dynamics of neurotransmitter release. Specifically, He and colleagues have shown that the power-law function using the < 0.1Hz frequency region better fits the fMRI power spectrum than exponential and log-normal functions. Accordingly, the power-law exponent, β, within the frequency range of interest (0.025 – 0.105Hz) was computed in subcortical regions (amygdala, hippocampus, thalamus, ventral and dorsal striatum), gray matter cortical regions, and white matter. We obtained the power-law exponent β by fitting a power-law function to the 0.025-0.105Hz frequency region of the power spectral

density.

The difference in spectral properties between patients with glioblastoma and reference subjects was examined using a two-sided Wilcoxon rank sum test (significance level of $p < 0.05$). A two-sample t-test (significance level $p < 0.05$) was used to compare power-law exponents between two groups based on their mutational status, and we excluded patients with missing data for this analysis (FIG. 9A, FIG. 9B). A cross-over frequency was identified for the gene with a statistically significant difference in spectra based on mutational status, and a two-sided Wilcoxon rank sum test was used to evaluate the differences in fALFF at the two frequency bands between the two groups based on their mutational status. To test the association between clinical comorbidities and the power-law exponent, patients were ranked based on their power-law exponents averaged across cortical voxels, and the top and bottom 20% were selected. The Fisher's exact test (MATLAB function *fishertest*) was used to evaluate the nonrandom association between the power-law exponent and the presence of comorbidities. Additionally, a linear regression model (MATLAB function *fitlm*) was used to evaluate the association between the number of clinical comorbidities and power-law exponents.

Survival analysis was performed by first median-splitting patients into two groups (N = 95 vs. 94) based on their overall survival (time of diagnosis to death). The average power spectra for each group were computed, and cross-over frequency points (0.045Hz and 0.085Hz) were identified. Using these frequency points, a voxel-wise % difference in each frequency-band specific fALFF (0.025-0.045Hz, 0.045-0.085Hz, 0.085-0.105Hz) was computed by averaging fALFF maps for all patients in each group.

Next, patients were median-split into two groups based on the averaged fALFF values in the gray matter, and the log-rank test was used to compare Kaplan-Meier survival curves. Additionally, univariate regression analysis was used to evaluate the effects of variables (age, sex, tumor volume, KPS, MGMT methylation status, surgical status, and fALFF in gray matter) on survival using Cox proportional hazards regression (MATLAB function *coxphfit*). Variables with significant p-values in the univariate analysis were included in a multivariate

model using the Cox regression proportional hazard model. Bonferroni corrected p-values indicate statistical significance. All statistical analyses were performed in Matlab.

FIGS. 6A, 6B, and 6C illustrate brain-wide power-law exponent changes seen in patients with glioblastoma. The power-law exponent, β, averaged over the whole brain was different in the patient group as compared to the reference group (FIG. 6A). FIG. 6B shows power spectra averaged over cortical gray matter, subcortical gray matter, and white matter. Gray matter (cortical + subcortical) median β values ranged from 0.6 to 1.2 and 0.44 to 0.86 in reference subjects and glioblastoma patients, respectively (FIG. 6C). In cortical networks, β was greatest in the visual network and least in the cingulo-opercular network. Group differences in β were significant across all regions (FIGS. 6B and 6C; Wilcoxon rank-sum test, $p < 1e\text{-}4$ for all regions). We observed no clear evidence of focality or resting state network specificity in averaged data (FIG. 6C). We observed no clear evidence of focal or resting state network (RSN) specific aberrancy in tumor patients compared to the reference group, based on our averaged data (FIG. 6C). The RSNs we evaluated included cingulo-opercular network, salience network, somatomotor network, among others. Our observations were based on the averaged data across these networks.

FIGS. 7A, 7B, 7C, and 7D illustrate differences in frequency-specific fALFF between the OASIS subjects and glioblastoma patient datasets. fALFFs between 0.025 – 0.105Hz, with a 0.01Hz interval, were computed in each subject in each group and averaged across the subjects. The shaded boxes within the row of eight boxes shown on each panel indicate a frequency-specific fALFF (0.01Hz interval between 0.025 – 0.105 Hz). fALFF evaluated over the entire spectral range between 0.025 Hz and 0.105 Hz was significantly lower in patients compared to the reference cohort in both gray and white matter (FIG. 7A). FIG. 7B shows that this effect was largely driven by the lowest frequencies. Restricting fALFF to frequencies centered around 0.06 Hz yielded no group differences in either gray or white matter (FIG. 7C). In contrast, fALFF evaluated at frequencies > 0.075 Hz was greater in patients in both gray and white matter and this effect was more pronounced in white matter (FIG. 7D). These results suggest that spontaneous BOLD fluctuations in glioblastoma patients include

more activity conventionally regarded as “noise” (discussed further below). Conventional fMRI studies assume that fluctuations above 0.1Hz have greater physiological noise components than neural-activity-relevant signals.

Previous work has demonstrated close associations between epigenetic regulations and tumor progression. To examine such associations in our data, we evaluated β in patients categorized according to the methylation status of MGMT as well as three other somatic mutations commonly seen in glioblastoma, (EGFR, PTEN, and TERT; Table 1). β differed significantly only based on MGMT mutation status, with the presence of a mutation leading to a decrease in β ($p = 0.017$, two-sample t-test). To further investigate this difference, we carried out analyses similar to those shown above, contrasting patients according to MGMT mutational status. The average voxel-wise β was subtly smaller in patients with methylated MGMT (FIG. 8A). Moreover, the average power spectrum was significantly flatter in the unmethylated group (FIG. 8B). Spectral band analyses parallel to those in FIGS. 7A, 7B, 7C, and 7D showed that patients with methylated MGMT exhibited decreased fALFF at lower frequencies and increased fALFF at higher frequencies. The direction of these MGMT-dependent findings suggests that methylation exacerbates the spectral effects caused by glioblastomas. Interestingly, methylation is associated with increased survival in treated patients. This apparent discrepancy is discussed below.

Brain function is not independent of other organs and systems in the body. Accordingly, we hypothesized that clinical comorbidities would also be associated with spectral changes in spontaneous BOLD fluctuations. To test this hypothesis, we ranked patients according to β averaged over cortical gray matter. FIG. 9A shows results comparing patients in the quintile with the flattest spectra vs. the quintile with the steepest spectra. Comorbid conditions were more prevalent in patients with the flattest spectra, i.e., smaller β (FIG. 9A). We found a statistically significant negative correlation between the number of comorbid conditions and their averaged βs across the cortical gray matter voxels (FIG. 9B, $p < 0.005$). These results suggest that clinical comorbidities influence the spectral content of BOLD fluctuations similarly to glioblastomas.

Significant differences in the spectral properties of the patient vs.

reference cohorts raise the possibility that these effects are biomarkers of the brain's functional status and, hence, prognosis. Our findings thus far show that lower-frequency fALFF is decreased while higher-frequency fALFF is increased in glioblastoma patients. Similar findings were observed in association with clinical comorbidities in the patient group. Based on these observations, we hypothesized that the spectral properties of spontaneous BOLD fluctuations carry prognostic significance. To examine this hypothesis, we divided the patients into two subgroups based on overall survival of greater than vs. less than 14 months, the median overall survival in our patient cohort. Power spectra averaged over the cortical gray matter were evaluated in each group (FIG. 10A). FIG. 10B shows significant fALFF differences in the two groups broken down by spectral band (two-sided Wilcoxon rank-sum test, $p < 0.0001$). FIG. 10C shows voxel-wise fALFF in the two groups evaluated over three spectral bands. In parallel, we computed Kaplan-Meier survival curves based on cortical gray matter fALFF evaluated in the same spectral bands. Significant differences in median survival were found for the lowest (0.025-0.045Hz) and highest (0.085-0.105Hz) frequency bands (first and third panels in FIG. 10D; log-rank test, $p = 0.038$ and $p = 0.017$, respectively). Univariate and multivariate Cox regression results are shown in Table 2. Frequency-specific fALFF was a significant prognostic factor even after accounting for age, tumor volume, MGMT methylation status, KPS, and surgical status.

Table 2. Univariate and multivariate survival analysis.

Characteristic	**Univariate Cox**		**Multivariate Cox**	
	HR (95% CI)	*p*	HR (95% CI)	*p*
Age at initial dx	1.03 (1.01, 1.04)	<1e-3	1.03 (1.01, 1.04)	<1e-3
CE volume (cm^3)	1.01 (1.00, 1.01)	0.003	1.01 (1.00, 1.01)	<1e-3
Sex	1.16 (0.86, 1.56)	0.327		
MGMT methylation	0.68 (0.51, 0.92)	0.013	0.38 (0.27, 0.53)	<1e-7
KPS (> 70)	0.33 (0.23, 0.49)	<1e-7	0.45 (0.29, 0.69)	<1e-3
Surgical Status (GTR/NTR/STR vs. LITT/Biopsy/None)	0.52 (0.38, 0.72)	<1e-4	0.49 (0.35, 0.69)	<1e-4

Cortical gray matter fALFF (0.025-0.045Hz) = High	1.36 (1.01, 1.81)	0.038	1.45 (1.01, 1.94)	0.014
Cortical gray matter fALFF (0.085-0.105Hz) = Low	1.43 (1.06, 1.91)	**0.018**	1.49 (1.11, 2.01)	**0.009**

Our principal finding is that glial tumors induce widely distributed changes in the spectral content of spontaneous BOLD fMRI fluctuations. These changes manifest as flatter power spectra (lower value of the power law exponent, β), and reduced gray matter fALFF relative to a reference cohort. Similar spectral findings were observed in association with MGMT promoter methylation status and several clinical comorbidities. Flattened spectra, relatively depressed lower-band fALFF, and elevated higher-band fALFF were associated with shortened survival, i.e., unfavorable prognosis. As far as we are aware, this is the first study to focus on the spectral properties of spontaneous BOLD fMRI fluctuations in glioblastoma patients and to evaluate spectral properties as a prognostic indicator. The MGMT finding is anomalous as this biomarker has been associated with longer survival in treated patients. This apparent discrepancy is discussed more fully below.

Our findings are consistent with the perspective that glioblastoma is a brain-wide disease. Previous studies have demonstrated that tumor cells often infiltrate the entire brain and brainstem. Cerebrospinal fluid metabolomics differ between tumor patients and healthy controls. The global nature of rs-fMRI abnormalities in glioblastoma patients is also reflected in the resting state fMRI literature. Multiple studies have reported altered functional connectivity (FC) extending beyond the anatomical limits of the tumor. FC is used to map the representation of function within the brain and is calculated as the Pearson temporal correlation between pairs of time series extracted from regions of interest. Here, we evaluated BOLD fMRI fluctuations using a complementary approach, specifically, voxelwise analysis of resting state data in the temporal frequency domain. We find no evidence of lateralization. Direct comparison of

spectral properties in ipsi-lesional vs. contra-lesional hemispheres (excluding the tumor and the corresponding homotopic region) revealed no significant differences.

Regarding the significance of power spectrum flattening, it is well established that BOLD fMRI signals of neural origin normally exhibit a "1/f-like" spectral characteristic. Power at faster frequencies is attenuated by the kinetics of neurovascular coupling. Thus, in the reference cohort, power at low and high frequencies is concentrated in gray and white matter, respectively (FIG. 7). In other words, spontaneous BOLD fluctuations of neural origin are represented primarily at lower temporal frequencies. In practice, electronic noise and artifacts (principally generated by head motion) contaminate BOLD fMRI signals at all frequencies. Accordingly, measured power becomes increasingly dominated by variance of non-neural origin at frequencies > ~0.1 Hz. It is for this reason that functional connectivity studies conventionally limit the analysis to frequencies below ~0.1 Hz. These considerations imply that the flattening of the BOLD fMRI power spectrum reflects a relative loss of BOLD fluctuations of neural origin and, hence, represents a potential biomarker of impaired brain integrity. This perspective is supported by the observation that comorbidities in the present patient sample were associated with smaller β, i.e., flatter spectra. Similar considerations explain why attenuation of global FC strength is the most commonly reported finding in rs-fMRI studies of glioblastoma.

The pathophysiology responsible for flattening BOLD power spectra is as yet uncertain. One possibility is excess glutamate, the principal excitatory neurotransmitter in the brain. Glioma cells release excess glutamate into the CSF and extracellular fluid. Excess glutamate may shift the excitatory/inhibitory (E/I) balance throughout the brain towards hyperexcitability. Such a shift in E/I balance would be expected to disrupt neural processes giving rise to normal spontaneous BOLD activity and depressing power in the low-frequency end of the power spectrum. Conversely, administering midazolam, a GABAA receptor agonist, decreases the global E/I ratio, enhancing power in the low-frequency end of the power spectrum. Glutamate-induced hyperexcitability may also contribute to the high incidence (30-50%) of seizures in glioblastoma patients. In our data, seizures were significantly more prevalent in patients with smaller βs

(FIG. 5A). An alternative mechanism leading to flatter spectra is a shift of intrinsic time scales toward faster frequencies as a correlate of increased neural excitability. This mechanism occurs as a lateralized finding in temporal lobe epilepsy. Here, we posit that increased excitability occurs globally in brains with glioblastomas.

Reduced gray matter fALFF, a principal present finding (FIG. 7A), has been previously related to cognitive performance measures in nominally healthy individuals as well as patients with Alzheimer's disease. Other evidence demonstrates a tight link between impaired cognitive status and shortened survival in glioblastoma patients. Thus, there appears to exist a triple association between reduced gray matter fALFF (FIG. 7), impaired cognitive status, and shortened survival (FIG. 10) in patients with glioblastoma.

Perhaps the most salient feature in the present results is the negative prognostic value of spectral changes in glioblastoma patients. We previously reported that functional connectivity changes have prognostic value in glioblastoma patients. The present finding is distinct, based on spectral as opposed to connectivity analysis, and is an empirical finding about which we cannot be etiologically more specific. However, it is consistent with the observation that a variety of comorbid conditions are associated with flattened BOLD power spectra (FIG. 9). MGMT methylation was independently associated with flattened power spectra, particularly in white matter and the brainstem (FIG. 8C). One hypothesis is that epigenetic modulation of metabolism in glioblastoma may induce brain-wide changes through mechanisms such as paracrine signaling, thereby supporting tumor progression. This aligns with our present considerations and may indicate a poor prognosis. In practice, however, hypermethylation of the MGMT gene is associated with better prognosis in treated patients as it enhances sensitivity to alkylating agents and radiation therapy. Yet, the prognostic significance of MGMT methylation status in the absence of any therapy has not been reported.

Additional descriptions of the experiments and results described above are provided in Appendix A, the content of which is incorporated by reference in its entirety.

EXAMPLE 2 – SPECTRAL CHARACTERISTICS OF BOLD FLUCTUATIONS AND GLUCOSE METABOLISM ACROSS THE ADULT LIFESPAN

Brain metabolism and measures of physiologic integrity decline with age in a manner parallel to numerous other physiologic measures. We evaluated changes in the spectral slope (SS) of blood-oxygen-level-dependent (BOLD) fluctuations across the cortex using a cross-sectional group of 455 individuals aged 20 to 87 years.

The study included 455 participants from the adult lifespan Cambridge Centre for Ageing& Neuroscience (Cam-CAN) dataset. Exclusion criteria included suboptimal registration due to compromised structural scans or significant head motion. The demographics of our sample include an age range of 18 to 88 years (54.7 ± 18.5 yrs), comprising 276 males and 179 females. Inclusion criteria included cognitively healthy subjects without communication or mobility issues, substance abuse problems, and those eligible for MRI scans. MRI datasets were collected at a single site (MRC-CBSU) using a 3T Siemens TIM Trio scanner with a 32-channel head coil. T1w and T2w structural images and resting state scans were used in our analysis. The resting-state fMRI data included an 8-minute 40-second run (261 frames) acquired while participants rested with their eyes closed. A T2*-weighted echoplanar imaging (EPI) sequence was used to collect 261 volumes, each containing 32 axial slices with a slice thickness of 3.7mm, interslice gap of 0.74 mm for whole brain coverage (TR = 1970ms; TE = 30ms; flip angle = 78°; field of view (FOV) = 192x192mm; voxel-size = 3x3x4.44mm).

Cognitively unimpaired adults without evidence of brain Alzheimer's Disease (AD) pathology were recruited from Washington University in St. Louis community and the Knight Alzheimer Disease Research Center. Data from a total of 94 participants from this dataset were selected and divided into two groups: 30 young adults (ages 25-45 years; 16 males, 14 females); and 64 older adults (ages 65-85yrs; 32 males, 32 females). All participants had undergone Positron Emission Tomography (PET) imaging using a Siemens ECAT HR+ scanner. The protocol included a single 18F-FDG scan, following a slow intravenous injection of 5 mCi FDG, and two sets of ^{15}O PET scans. The final 20 minutes (40-60 minutes post-injection) of dynamic acquisition of the FDG images

were summed and converted to SUVR measurements relative to the whole brain to assess the cerebral metabolic rate of glucose (CMRGlc). Each ^{15}O PET session consisted of two sessions of three scans to measure cerebral blood volume (CBV), cerebral blood flow (CBF), and cerebral metabolic rate of O_2 ($CMRO_2$). Participants were instructed to remain awake with their eyes closed throughout the scans.

Initial fMRI preprocessing included compensation for slice-dependent time shifts and rigid body correction of head movement within and across runs. The preprocessed data were then resampled to align the structural data in $(3mm)^3$ atlas space using a composition of initial affine transform and a warping map (computed using the Advanced Normalization Tools (ANTs) registration) connecting the fMRI volumes with the T1w structural image. Motion correction was included in the final resampling to generate a volumetric time-series in $(3mm)^3$ atlas space. Further preprocessing steps included the removal of voxel-wise linear trends from each fMRI run, temporal low-pass filtering to retain frequencies below 0.15Hz, and regression of nuisance waveforms. These regressors included six head motion time-series, average signals from CSF regions, and the signal evaluated over the whole brain (global signal regression). Finally, spatial smoothing was applied (6mm full width at half maximum Gaussian blur in each direction).

To accurately estimate metabolic activity specific to a tissue type, partial volume correction (PVC) is essential owing to the limited spatial resolution of PET scans. The necessity arises from both the “tissue fraction” and the “point spread function” effects. Here, we employed a parcel-based approach for PVC, using Schaefer’s 200 parcellation scheme, presuming that each parcel exhibits a distinct and uniform activity level. A region-based, symmetric geometric transfer matrix framework for PVC was used, processing both PET images and parcel maps to compute a scalar activity estimate for each parcel. The PET images analyzed included CMRglc, CBF, and $CMRO_2$.

Resting state networks (RSNs) are hierarchically organized at multiple levels of granularity. In this study, cortical parcellations were obtained and resampled to the $(3mm)^3$ atlas space. For analyses involving generalized additive models (GAMs), we used the 300-parcellation scheme. From these 300

parcels, regions with a low signal-to-noise ratio (SNR), comprising the medial prefrontal cortex and anterior/ventral portions of the temporal lobe, were excluded. These regions were mainly associated with the limbic network as defined in Schaefer's 17 networks, reducing the number of parcels to 271 for analysis. For comparing spectral slope maps with metabolic measures from the AMBR dataset, which was processed for PVC using the 200-parcellation scheme, we also used the 200-parcellation scheme.

We computed the PSD from the lagged autocovariance function by employing a cosine-based Fourier transform ('Wiener-Khinchin theorem') to allow for the exclusion of high-motion frames. First, we computed a scaled temporal lag q associated with each lag m ($q = (m-1)*TR/30$), where TR represents the sampling interval, and 30 serves as a normalization factor for this analysis. The autocovariance values were adjusted by an exponential decay factor ($\exp(-0.5q^2)/n$) to account for the decrease in signal similarity with increasing time lags. This exponential decay factor is based on the temporal weighting factor q as well as the number of valid frame pairs n, thereby ensuring the analysis considers only those frames that are relatively *motion-free* (we use the term "motion-free" loosely, as these frames are still subject to head motion, albeit less so than the censored frames). Finally, a cosine transform was applied to the adjusted lagged autocovariance function for each voxel, yielding the PSD for each voxel.

BOLD fluctuations exhibit a scale-free activity. In the current study, we compared the "fitness" of the spectral slope between fitting the slope in log-log vs. log-normal function by evaluating R-squared values. Log-normal functions consistently yield higher R-squared values compared to those derived from the log-log functions. Accordingly, in the present study, we defined spectral slope as the negative of the first derivative of the slope fitted to the logged power vs. frequency in its natural scale.

Statistics for generalized additive models (GAMs) were performed using RStudio 2023.12.1+402 "Ocean Storm" and R 4.3.3. The current study expands on GAMs to characterize the impacts of aging, seen as part of continuing development/lifespan changes. GAMs are advantageous for the flexibility in modeling both linear and non-linear relationships between independent and

dependent variables. GAMs were fit with parcel-specific spectral slope as the dependent variable, including age as a smooth term and sex and in-scanner head motion as linear covariates. Models for each parcel were evaluated using thin plate regression splines as the smooth term basis set, applying the restricted maximal likelihood approach for smoothing parameters and limiting the maximum basis complexity (k) to 4. The significance of the association between spectral slope and age for each parcel was assessed using an analysis of variance (ANOVA), contrasting the full model (including both age and covariates) with a reduced model (only including covariates). The difference in the explained variance between the full model and the reduced model was denoted as the age-specific R^2. A significant result indicates a substantial reduction in residual deviance when age is included, as determined using the chi-squared test statistic. The p-values from the ANOVA across all parcel-specific GAMs were adjusted using the FDR correction. The threshold for statistical significance was set at $P_{FDR} < 0.05$.

We evaluated whether the extent to which spectral slope changed with age correlated spatially with “normative” CMRGlc topography. The “normative” CMRGlc topography was defined by the average baseline CMRGlc of young adults, corrected for PVC across Schaefer’s 200 parcels in the AMBR dataset. The correlation coefficient was computed between the age-specific R^2 values (comparing the full GAM model against the reduced GAM model) and the “normative” CMRglc map. The association between these two spatial maps was quantified with Spearman’s correlation, a non-parametric, rank-based method that does not depend on the assumption of normality.

The fuzzy-c-means clustering analysis was conducted in MATLAB 2023b. The *predict* function in R used for the full GAM model outputs the smooth function for age, which function represents the lifespan trajectory of each parcel’s spectral slope. Observing distinct patterns in each parcel’s lifespan trajectory showing varying levels of linearity, we applied fuzzy c-means clustering to assign a weighted membership between zero and one to each parcel’s trajectory. First, to determine the optimal cluster number, *fcm* was evaluated by incrementally increasing the cluster count (N = 2 - 15). Options used for *fcm* were as follows: the exponent of the fuzzy partition matrix was set

to 5 to allow a greater degree of overlap; the maximum iteration count was set to 10,000; the default value for the minimum objective function improvement between two consecutive iterations was used (1e-5); Euclidean distance was used as a distance metric. Subsequently, for each cluster number, a silhouette score was computed by first converting the weighted membership into a binary format using a winner-take-all analysis. Two clusters resulted in the highest silhouette score. Thus, N = 2 was used to cluster the trajectories and their corresponding cortical regions.

We evaluated whether clustering based on aging trajectories aligned with well-known resting state networks (RSNs). Considering their extensive work on precision functional mapping and an in-depth analysis of RSNs and their functions, comparing our clustering results with external RSN maps was deemed suitable. Specifically for this analysis, we leveraged the publicly available probabilistic mapping of the RSN data. First, the probabilistic RSN map was thresholded at 50%, ensuring that only regions with a high probability of belonging to an RSN were considered. Next, we computed a dot product between the thresholded RSN map and fuzzy c-means weighted cluster maps for both clusters (*dot-cluster1* vs. *dot-cluster2*). The difference between these two dot product maps (*difference map* = *dot-cluster2* – *dot-cluster1*) was computed to evaluate regions with greater association with either cluster. Based on this difference map, we counted the number of voxels that exhibited greater association with cluster 2 (*difference map* > 0) and with cluster 1 (*difference map* < 0). Finally, we computed the ratio of these voxel counts to ascertain which cluster had a greater representation in each RSN. A ratio greater than 1 indicates a higher voxel count in the corresponding RSN that aligns with the atrophy trajectory observed in cluster 2 compared to cluster 1.

The “youthful pattern” analysis, where individual brain metabolism (fludeoxyglucose and oxygen metabolism) and cerebral blood flow (CBF) maps were compared to the corresponding group maps from a young adult cohort using Spearman rank correlation was used. Extending this approach, we defined the spectral slope (SS) Youthful Index by evaluating the Spearman correlation between individual SS maps and the averaged SS maps from younger individuals (<45 yrs) in the CamCAN dataset. For outlier analysis, we identified

subjects whose SS youthful indices were greater than 3 scaled median absolute deviations from the median across all individuals in the CamCAN dataset. These outliers, represented as red dots and outlined with a red dashed box in FIG. 14A, are also highlighted in FIG. 14B, FIG. 14C, and FIG. 14D.

SS maps were additionally compared with averaged metabolic ($CMRGlc/CMRO_2$) and hemodynamic (CBF) maps from individuals under 45 years in the AMBR dataset. The objective of this analysis was twofold: 1) to evaluate changes in SS topography with aging and 2) to assess its similarity and changes in its similarity to "youthful" $CMRGlc/CMRO_2$/CBF maps with aging.

To determine whether outliers identified by the SS Youthful Index were driven by potentially confounding factors including gray matter volume, head motion, and sex differences, we performed further analysis. Gray matter volume for each individual was quantified using FSL FAST segmentation, which segments the atlas-registered individual's T1w image into three tissue types: gray matter, white matter, and CSF. We calculated the individual-specific gray matter volume by summing the number of segmented gray matter voxels in $(3mm)^3$ atlas space. Head motion was assessed using the realignment procedure. Briefly, this measure averages the changes in head displacement and rotation in quadrature. Considering the greater variability observed among older subjects, we specifically included individuals aged over 45 years. A qualitative assessment of the relationship between these confounding variables and the SS Youthful Index was performed by plotting the individual indices against their gray matter volume and head motion. Histograms of both non-outliers and outliers were plotted, grouped by sex, to visually inspect distribution differences. To quantitatively determine if any of these variables explain the difference between individuals in the outlier vs non-outlier groups, we fitted a linear regression model with the binarized SS Youthful Index as the response variable. Gray matter volume (GMV) and head motion (HM) were used as continuous predictor variables, and sex as a categorical predictor variable:

$$SS\ Youthful\ Index \sim \beta_o + \beta_1 GMV + \beta_2 HM + \beta_3 sex$$

Results

We evaluated changes in the spectral slope (SS) of BOLD fluctuations

across the cortex using a cross-sectional group of 455 individuals aged 20 to 87 years. SS, computed using linear regression of log power against frequency within the 0.015-0.145 Hz band, indexes the relative prevalence of slow vs. fast BOLD activity. Prior works have demonstrated a correlation between steeper slopes (i.e., greater coherence at the lowest frequencies within the infraslow frequency range) and higher glucose metabolism. To characterize age-related SS changes across cortical parcels, we fit parcel-specific generalized additive models (GAMs), accounting for age as a smoothing term and including sex and head motion as linear covariates. Each GAM estimates smooth age-related functions, charting the parcel-wise trajectory of changes in SS with age. In the present work, we first assessed the association between the degree of age effect on SS and the cerebral metabolic rate of glucose (CMRGlc) using an independent metabolic dataset (AMBR dataset). We then identified distinct trajectories of SS changes across cortical regions. Finally, we examined age-related changes in the youthful pattern of SS topography as well as its relation to youthful metabolic measures.

To visualize SS changes with increasing age, we binned data into three age groups (20-40, 41-65, and 66-87 years). FIG. 11A shows BOLD fluctuations sampled from the same ROIs in two subjects in both time and frequency domains. FIG. 11B illustrates the average power spectra, computed by averaging across all cortical voxels and participants within each age group. SS was defined as the negative of the first derivative of the slope fitted to the logged power (FIG. 11B; right panel). FIG. 11C demonstrates the spatial patterning of SS changes from youth to old age. Warmer hues indicate a steeper SS, reflecting a greater prevalence of slow over fast activity within the infra-slow frequency range. The steepest spectral slopes were observed in medial and lateral parietal, prefrontal, and visual cortices. This topography remained consistent across all age groups, suggesting that, despite a general flattening observed in the brain, major features of SS topography are preserved with age.

To evaluate aging-related SS changes across cortical regions, we modeled parcel-specific GAMs, including age as a smooth term and sex/head motion as linear covariates. The regional magnitude of age effects was assessed using age-specific R^2, which measures the differences in explained variance

between the full model (with age) and the reduced model (without age) (FIG. 12A). Age-specific R^2 varied from 0 to 0.12, where 0 indicates that SS change is attributable to covariates other than age. High age-specific R^2 values denote regions where age heavily contributes to SS changes. A significant change in SS with age was observed in 82% of cortical parcels ($P_{FDR} < 0.05$). Significant age effects were found in lateral and medial prefrontal regions, specific parietal regions, the posterior cingulate cortex, and the medial surface of the visual cortex. Interestingly, the age effect on spectral slope mirrored brain CMRGlc topography (FIG. 12B, FIG. 12C; Spearman's correlation $\rho = 0.66$, $p = 1.40e\text{-}24$), with brain regions with greater glucose metabolism showing greater age-effect on SS changes (FIG. 12C).

Visualization of age-trajectory fits across regions revealed either consistent flattening of spectral slope throughout life or no decline until mid-adulthood, followed by marked and continuous flattening. We used fuzzy c-means clustering to systematically group these varying trajectories across cortical parcels. Silhouette score analysis indicated that two clusters were optimal. Whereas most cortical regions exhibited continuous SS flattening (FIG. 13A), certain regions, particularly those coinciding with auditory/cingulo-opercular/salience networks, exhibited flattening starting in mid-adulthood (FIG. 13B, FIG. 13C). Noteworthy regions within Cluster 2 include dorsal anterior cingulate cortex (dACC), frontal operculum, supplementary motor area (SMA), supramarginal gyrus (SMG), inferior frontal gyrus (IFG), pars marginalis of the cingulate gyrus, and the mesial surface of the visual cortex.

To demonstrate changes in SS topography with age, we use the "youthful pattern" approach. Here, the SS Youthful Index is defined as a Spearman's correlation between individuals' SS maps and the averaged SS_{young} map (FIG. 14A). The youthful pattern of SS topography generally persists across the lifespan. However, the SS Youthful Index shows increasing variability with increasing age. There is a topographical similarity between individual SS maps and the normative CMRGlc map (FIG. 14B). The correlation is less apparent with $CMRO_2$ (FIG. 14C) and closer to zero with CBF (FIG. 14D).

Importantly, a distinct subset of older individuals displays significantly weaker or even negative SS Youthful Indices (i.e., less than three scaled median

absolute deviations from the median). We label these individuals as outliers (red dots in FIG. 14A) for further analysis. Interestingly, these outliers also exhibit weaker correlations with $CMRGlc_{young}$ and $CMRO2_{young}$ (FIG. 14B, FIG. 14C). A similar trend is observed with CBF, although not as pronounced FIG. 14D).

Older subjects typically exhibit greater gray matter atrophy and increased head motion. Accordingly, we hypothesized that the identified outliers (red dots in FIG. 14A) would demonstrate smaller cortical volume and/or higher head motion. Additionally, considering previous findings that the adult female brain is metabolically more “youthful”, we assessed for sex differences between the outlier and non-outlier groups. Specifically, we focused on a group of middle-aged to elderly subjects (aged over 45 years) for this analysis.

No significant differences are observed in gray matter volume, head motion, or sex between these groups. In FIG. 15A and FIG. 15B, the overlays of black dots on red dots indicate comparable distributions of gray matter volume and head motion in both groups. The histogram in FIG. 15C shows no clear dominance of either sex in either group. To quantify our findings, we fit a linear regression model with gray matter volume and head motion as continuous variables and sex as a categorical variable, using the binarized SS Youthful Index as the response variable. The model did not significantly predict the SS Youthful Index ($R^2 = 0.0105$, $p = 0.369$), with none of the individual predictors showing statistical significance ($p = 0.122$ (gray matter volume), 0.750 (head motion), 0.262 (sex)). Our results suggest that among the middle-aged to elderly subjects in our cohort who exhibit a compromised SS Youthful Index, the observed effect is independent of gray matter atrophy, head motion, and sex.

Discussion

As the global population ages, there is a pressing need for accessible whole-brain imaging biomarkers to monitor and understand brain aging and health. Here, we propose that the spectral properties of rs-fMRI BOLD signals may serve as sensitive biomarkers of the neurometabolic aging process. fMRI has historically been primarily used for mapping task-based regional changes or identifying functional topographies using resting state functional connectivity (RSFC). Our current work focuses on a complementary approach to these

methods and evaluates age-related changes in BOLD signal spectra, with a particular focus on their relationship with cerebral metabolism.

Cerebral metabolism declines with age. We find that resting-state BOLD fMRI signal fluctuations typically exhibit a progressive spectral slope (SS) flattening with age, most prominently in cortical regions with high baseline glucose metabolism in younger individuals. There is, however, regional heterogeneity. While most cortical regions show a continuous SS flattening, some regions show a delayed onset of flattening starting in mid-adulthood. Specifically, regions overlapping with auditory, cingulo-opercular, and salience networks. Consistent with prior works, we report a topographical similarity between SS and CMRGlc. This is most consistent in young adults. SS Youthful Index analysis suggests that while SS topography maintains a youthful pattern with aging, a subset of older individuals deviate significantly from this pattern. Intriguingly, these subjects also exhibit reduced similarity between their SS topographies and the normative “youthful” pattern of metabolism. Moreover, inter-subject variability in both the SS Youthful Index and SS-CMRGlc similarity increases cross-sectionally with advancing age. These observations raise the question of whether the SS Youthful Index represents a biomarker of pathological neurometabolic aging.

Prior analyses of BOLD signal fluctuations have largely focused on the amplitude of low-frequency fluctuations (ALFF) and fractional ALFF (fALFF). Comparatively, fewer studies have focused on the spectral slope. ALFF quantitates the average power within a selected infra-slow frequency range (typically, <0.1 Hz). In contrast, fractional ALFF (fALFF) represents the relative prevalence of slow vs. fast activity. Accordingly, fALFF quantifies the proportion of infra-slow frequency activity relative to the full frequency spectrum (the range of measurable frequencies depends on the volume TR and fMRI run duration). Spectral slope characterizes the power spectrum in terms of a single number. This is possible because BOLD fluctuations are approximately scale-free, i.e., exhibit a 1/f-like power spectrum. Thus, the SS measure captures information similar to fALFF, although evaluated at a finer resolution.

The physiological significance of spectral slope flattening follows from the notion that infraslow frequencies (nominally, < 0.1Hz) primarily reflect signals of

neural origin, whereas faster frequencies represent artifacts, including thermal noise and head motion. As head motion manifests as intermittent burst noise, its spectrum is theoretically white, as is that of thermal noise. In contrast, direct measurements show that BOLD fMRI signals are very attenuated at frequencies greater than 0.2 Hz. Thus, BOLD power spectra generally assume the characteristic of a 1/f-like spectrum superimposed on a flat noise floor. Hence, the spectral slope (SS) indexes the extent to which BOLD fMRI fluctuations are of neural- as opposed to non-neural origin. Empirically, in glioblastoma patients, an increased proportion of high vs. low-frequency rs-fMRI BOLD activity is associated with compromised brain integrity. Here, we extend this principle to aging.

The underlying physiology defining the spectral slope of the BOLD signal, as well as its changes, are as yet uncertain. Despite this limited understanding, prior works have shown that the spectral properties of rs-fMRI signals depend on tasks, correlate with cerebral glucose metabolism, and are functionally organized. Intriguingly, regions with steeper spectral slopes (i.e., longer intrinsic timescales) exhibit stronger functional connectivity across extensive regions and spatially correspond with higher baseline CMRGlc (FIG. 14B). This circumstantial evidence suggests a potential relationship between the required metabolic supply and the maintenance of cellular or synaptic dynamics engaging in large-scale circuits over multiple timescales. Aging affects this process, perhaps due to the simplification of neuronal architecture (e.g., reduced arborizations and dendritic length, decreased spine numbers), accumulation of DNA damage and mutations, and inefficiencies in DNA repair processes. Accordingly, it is conceivable that aging-related degradation manifests as spectral slope flattening of BOLD signals.

Importantly, spectral slope flattening is more pronounced in regions with higher baseline CMRGlc. This may be because regions characterized by higher glucose metabolism have greater complexity underlying processes, and the more complex the system, the more it is predisposed to errors. For instance, hub-like areas, as defined by stronger whole-brain FC, are more likely to comprise a greater number of interdependent individual processes. Upkeeping activities in these regions would not only be metabolically costly but also

complex due to the need to maintain and repair each process as well as their interconnections. Consequently, age-related degradation and pathology would have a greater effect in such cortical regions. This hypothesis is further supported by previous observations that Aβ deposition is more commonly found in cortical hubs.

Regions overlapping auditory, cingulo-opercular, and salience networks exhibit a delayed onset of SS flattening starting mid-adulthood (FIG. 13B, FIG. 13C). These resting state networks are associated with intrinsic alertness, specifically relating to goal-directed behavior and responsiveness to environmental stimuli. Intriguingly, the environmental complexity has been shown to differentially affect dendritic branching across different lobes. Accordingly, the observed resilience may be due to sustained external feedback (e.g., social interactions) into mid-adulthood, which typically decreases with advancing age. From an evolutionary perspective, maintaining intrinsic neuronal timescales of these regions may also be more advantageous. Possibly related, the onset of morphological changes in neurons exhibits regional variability.

The “youthful pattern” of spectral slope topography is generally maintained across the lifespan. However, a subset of older individuals shows weaker and even negative SS Youthful Index values (FIG. 14A). Importantly, these outliers do not associate with cortical volume, head motion, or sex differences. However, these outliers may exhibit differences in cortical thickness, white matter hyperintensities, or other potential biomarkers of age-related pathology. While all participants included in this work are cognitively normal (as defined by MMSE score greater than 24), cognitive normality alone cannot rule out the presence of subjects with asymptomatic neuropathology. The appearance of abnormal biomarker values often precedes the onset of clinical symptoms by several years. Importantly, studies of normal aging are confounded by the failure to exclude participants positive for preclinical biomarkers. Hence, the outlier subset in our sample may exhibit covert neuropathology.

We propose a conceptual framework in which age-related biomarkers of neuropathology are characterized by change points at which the range of observed values progressively increases with age (FIG. 16). In some cases, pathology leads to decreased values (e.g., hippocampal volume, cortical

thickness). In other cases, pathology leads to increased values (e.g., white matter hyperintensities, PiB-PET, CSF p-tau). In both cases, the variance of the biomarker values within the group increases with age: some subjects exhibit the normative or youthful state, whereas some subjects deviate significantly from this youthful baseline. Within this framework, the spectral slope of rs-fMRI BOLD signals serves as a marker sensitive to pathological neurometabolic aging.

It should be appreciated by those of skill in the art that the techniques disclosed in the examples herein represent approaches the inventors have found function well in the practice of the present disclosure and thus can be considered to constitute examples of modes for its practice. However, those of skill in the art should, in light of the present disclosure, appreciate that many changes can be made in the specific embodiments that are disclosed and still obtain a like or similar result without departing from the spirit and scope of the present disclosure.

Claims

What is claimed is:

1. A system to identify a brain disorder in a patient, the system comprising at least one processor configured to:
    a. receive a resting-state functional magnetic resonance image (rs-fMRI) dataset obtained from a brain of the patient;
    b. transform the rs-fMRI data set into a power spectral density (PSD) dataset;
    c. transform at least a portion of the PSD dataset corresponding to at least one region of the brain of the subject into a power-law exponent (β) dataset and at least two fractional amplitudes of low-frequency fluctuations (fALFF) datasets, wherein the at least two aALFF datasets are selected from a lower-frequency fALFF dataset computed from a lower-frequency portion of the PSD dataset and a higher-frequency fALFF computed from a higher-frequency portion of the PSD dataset, or a fALFF dataset computed from all frequencies of the PSD dataset;
    d. compare the power-law exponent (β) dataset and at least two fALFF datasets to corresponding reference power-law exponent (β) datasets and at least two reference fALFF datasets obtained from healthy control subjects;
    e. identify the brain disorder based on differences in the power-law exponent (β) dataset and at least two fALFF datasets relative to the corresponding reference power-law exponent (β) dataset and at least two reference fALFF datasets; and
    f. communicate the brain disorder to a display device of a practitioner.
2. The system of claim 1, wherein the rs-fMRI dataset comprises a plurality of time-series of blood-oxygen-level-dependent (BOLD) signals, each time-series obtained from a voxel within the brain of the subject.

3. The system of any preceding claim, wherein the PSD dataset comprises a series of spectral powers and corresponding BOLD signal frequencies over a pre-specified range of BOLD signal frequencies for each voxel of the rs-fMRI dataset.

4. The system of any preceding claim, wherein the power-law exponent (β) dataset comprises a plurality of power-law exponents (β) corresponding to the plurality of voxels of the rs-fMRI dataset, each power-law exponent (β) obtained by fitting a power-law function to each PSD of at least a portion of the PSD dataset.

5. The system of any preceding claim, wherein the pre-specified range of BOLD signal frequencies comprises a range of less than about 0.100 Hz.

6. The system of any preceding claim, wherein the pre-specified range of BOLD signal frequencies comprises a range from about 0.025 Hz to about 0.105 Hz.

7. The system of any preceding claim, wherein the brain disorder is identified in the patient for the differences comprising at least one of:

    a. power-law exponents (β) lower than the corresponding reference power-law exponents (β);

    b. fALFFs over a range of BOLD signal frequencies of less than about 100 Hz are lower than the corresponding reference fALFFs; and

    c. fALFFs over a range of BOLD signal frequencies from about 0.025 Hz to about 0.105 Hz are lower than the corresponding reference fALFFs.

8. The system of any preceding claim, wherein the processor is further configured to:

    a. calculate a predicted prognosis for the subject based on the differences in the at least one fALFF dataset relative to a corresponding at least one reference fALFF dataset; and

    b. communicate the predicted prognosis to the display device of the practitioner.

9. The system of claim 8, wherein the predicted prognosis comprising a shortened survival probability is calculated for at least one of:

    a. the fALFF dataset obtained from a lower-frequency range of BOLD signal frequencies from about 0.025 Hz to about 0.045 Hz is lower than the corresponding reference fALFF dataset; and

    b. the fALFF dataset obtained from a higher-frequency range of BOLD signal frequencies from about 0.085 Hz to about 1.05 Hz is higher than the corresponding reference fALFF dataset.

10. A computer-implemented method to identify a brain disorder in a patient, the method comprising:

    a. receiving, at a computing device, a resting-state functional magnetic resonance image (rs-fMRI) dataset obtained from a brain of the patient;

    b. transforming, using the computing device, the rs-fMRI data set into a power spectral density (PSD) dataset;

    c. transforming, using the computing device, at least a portion of the PSD dataset corresponding to at least one region of the brain of the subject into a power-law exponent (β) dataset and at least two fractional amplitudes of low-frequency fluctuations (fALFF) datasets, wherein the at least two aALFF datasets are selected from a lower-frequency fALFF dataset computed from a lower-frequency portion of the PSD dataset and a higher-frequency fALFF computed from a higher-frequency portion of the PSD dataset, or a fALFF dataset computed from all frequencies of the PSD dataset;

    d. comparing, using the computing device, the power-law exponent (β) dataset and at least two fALFF datasets to corresponding reference power-law exponent (β) datasets and at least two reference fALFF datasets obtained from healthy control subjects;

    e. identifying, using the computing device, the brain disorder based on differences in the power-law exponent (β) dataset and at least

two fALFF datasets relative to the corresponding reference power-law exponent (β) dataset and at least two reference fALFF datasets; and

f. communicating, using the computing device, the brain disorder to a display device of a practitioner.

11. The method of claim 10, wherein the rs-fMRI dataset comprises a plurality of time-series of blood-oxygen-level-dependent (BOLD) signals, each time-series obtained from a voxel within the brain of the subject.

12. The method of any one of claims 10 - 11, wherein the PSD data set comprises a series of spectral powers and corresponding BOLD signal frequencies over a pre-specified range of BOLD signal frequencies for each voxel of the rs-fMRI dataset.

13. The method of any one of claims 10 - 12, wherein the power-law exponent (β) dataset comprises a plurality of power-law exponents (β) corresponding to the plurality of voxels of the rs-fMRI dataset, each power-law exponent (β) obtained by fitting a power-law function to each PSD of at least a portion of the PSD dataset.

14. The method of any one of claims 10 - 13, wherein the pre-specified range of BOLD signal frequencies comprises a range of less than about 0.100 Hz.

15. The method of any one of claims 10 - 14, wherein the pre-specified range of BOLD signal frequencies comprises a range from about 0.025 Hz to about 0.105 Hz.

16. The method of any one of claims 10 - 15, wherein the brain disorder is identified in the patient for the differences comprising at least one of:

a. power-law exponents (β) lower than the corresponding reference power-law exponents (β);

b. fALFFs over a range of BOLD signal frequencies of less than about 100 Hz are lower than the corresponding reference fALFFs; and

c. fALFFs over a range of BOLD signal frequencies from about 0.025 Hz to about 0.105 Hz are lower than the corresponding reference fALFFs.

17. The method of any one of claims 10 - 16, wherein the processor is further configured to calculate a predicted prognosis for the subject based on the differences in the at least one fALFF dataset to corresponding at least one reference fALFF dataset.

18. The method of claim 17, wherein the predicted prognosis comprises a shortened survival probability is calculated for at least one of:

a. the fALFF dataset obtained from the lower-frequency range of BOLD signal frequencies from about 0.025 Hz to about 0.045 Hz is lower than the corresponding reference fALFF dataset; and

b. the fALFF dataset obtained from the higher-frequency range of BOLD signal frequencies from about 0.085 Hz to about 1.05 Hz is higher than the corresponding reference fALFF dataset.

19. A system to identify pathological neurometabolic aging in a patient, the system comprising at least one processor configured to:

a. receive a resting-state functional magnetic resonance image (rs-fMRI) dataset obtained from a brain of the patient;

b. transform the rs-fMRI data set into a power spectral density (PSD) dataset;

c. transform at least a portion of the PSD dataset corresponding to at least one region of the brain of the subject into a spectral slope (SS) dataset;

d. compare the SS dataset to a corresponding reference SS dataset obtained from age-matched healthy control subjects;

e. identify the pathological neurometabolic aging based on differences in the SS dataset relative to the corresponding reference SS dataset; and

f. communicate the pathological neurometabolic aging to a display device of a practitioner.

20. The system of claim 19, wherein the rs-fMRI dataset comprises a plurality of time-series of blood-oxygen-level-dependent (BOLD) signals, each time-series obtained from a voxel within the brain of the subject.

21. The system of any one of claims 19-20, wherein the PSD data set comprises a series of spectral powers and corresponding BOLD signal frequencies over a pre-specified range of BOLD signal frequencies for each voxel of the rs-fMRI dataset.

22. The system of any one of claims 19 - 21, wherein the SS dataset comprises a plurality of spectral slopes corresponding to the plurality of voxels of the rs-fMRI dataset, each spectral slope comprising a negative slope of a linear regression of log power against frequency from each PSD of the PSD dataset.

23. The system of any one of claims 19 - 22, wherein the at least one processor is further configured to transform the SS dataset and the corresponding reference dataset into an SS Youthful Index, the SS Youthful Index comprising a Spearman's correlation between the SS dataset and the corresponding reference SS dataset over a pre-specified range of BOLD signal frequencies.

24. The system of any one of claims 19 - 23, wherein the pathological neurometabolic aging is identified if the SS Youthful Index falls below a threshold value.

25. The system of any one of claims 19-24, wherein the threshold value comprises a value of the SS Youthful Index at least three scaled median absolute deviations below a median value of SS Youthful Indices obtained for a healthy control population.

26. The system of any one of claims 19-25, wherein the pre-specified range of BOLD signal frequencies comprises a range from about 0.015 HZ to about 0.145 Hz.

27. A computer-implemented method to identify pathological neurometabolic aging in a patient, the method comprising:

    a. receiving, at a computing device, a resting-state functional magnetic resonance image (rs-fMRI) dataset obtained from a brain of the patient;

    b. transforming, using the computing device, the rs-fMRI data set into a power spectral density (PSD) dataset;

    c. transforming, using the computing device, at least a portion of the PSD dataset corresponding to at least one region of the brain of the subject into a spectral slope (SS) dataset;

    d. comparing, using the computing device, the SS dataset to a corresponding reference SS dataset obtained from age-matched healthy control subjects;

    e. identifying, using the computing device, the pathological neurometabolic aging based on differences in the SS dataset and the corresponding reference SS dataset; and

    f. communicating, using the computing device, the pathological neurometabolic aging to a display device of a practitioner.

28. The method of claim 27, wherein the rs-fMRI dataset comprises a plurality of time-series of blood-oxygen-level-dependent (BOLD) signals, each time-series obtained from a voxel within the brain of the subject.

29. The method of any one of claims 27-28, wherein the PSD data set comprises a series of spectral powers and corresponding BOLD signal frequencies over a pre-specified range of BOLD signal frequencies for each voxel of the rs-fMRI dataset.

30. The method of any one of claims 27- 29, wherein the SS dataset comprises a plurality of spectral slopes corresponding to the plurality of voxels of the rs-fMRI dataset, each spectral slope comprising a negative slope of a linear regression of log power against frequency from each PSD of the PSD dataset.

31. The method of any one of claims 27- 30, further comprising transforming, using the computing device, the SS dataset and the corresponding reference dataset into an SS Youthful Index, the SS Youthful Index comprising a Spearman's correlation between the SS dataset and the corresponding reference SS dataset over a pre-specified range of BOLD signal frequencies.

32. The method of any one of claims 27- 23, wherein identifying the pathological neurometabolic aging based on differences in the SS dataset and the corresponding reference SS dataset further comprises identifying, using the computing device, the pathological neurometabolic aging if the SS Youthful Index falls below a threshold value.

33. The method of any one of claims 27-32, wherein the threshold value comprises a value of SS Youthful Index at least three scaled median absolute deviations from a median value of SS Youthful Indice obtained for a healthy control population.

34. The method of any one of claims 27-33, wherein the pre-specified range of BOLD signal frequencies comprises a range from about 0.015 HZ to about 0.145 Hz.

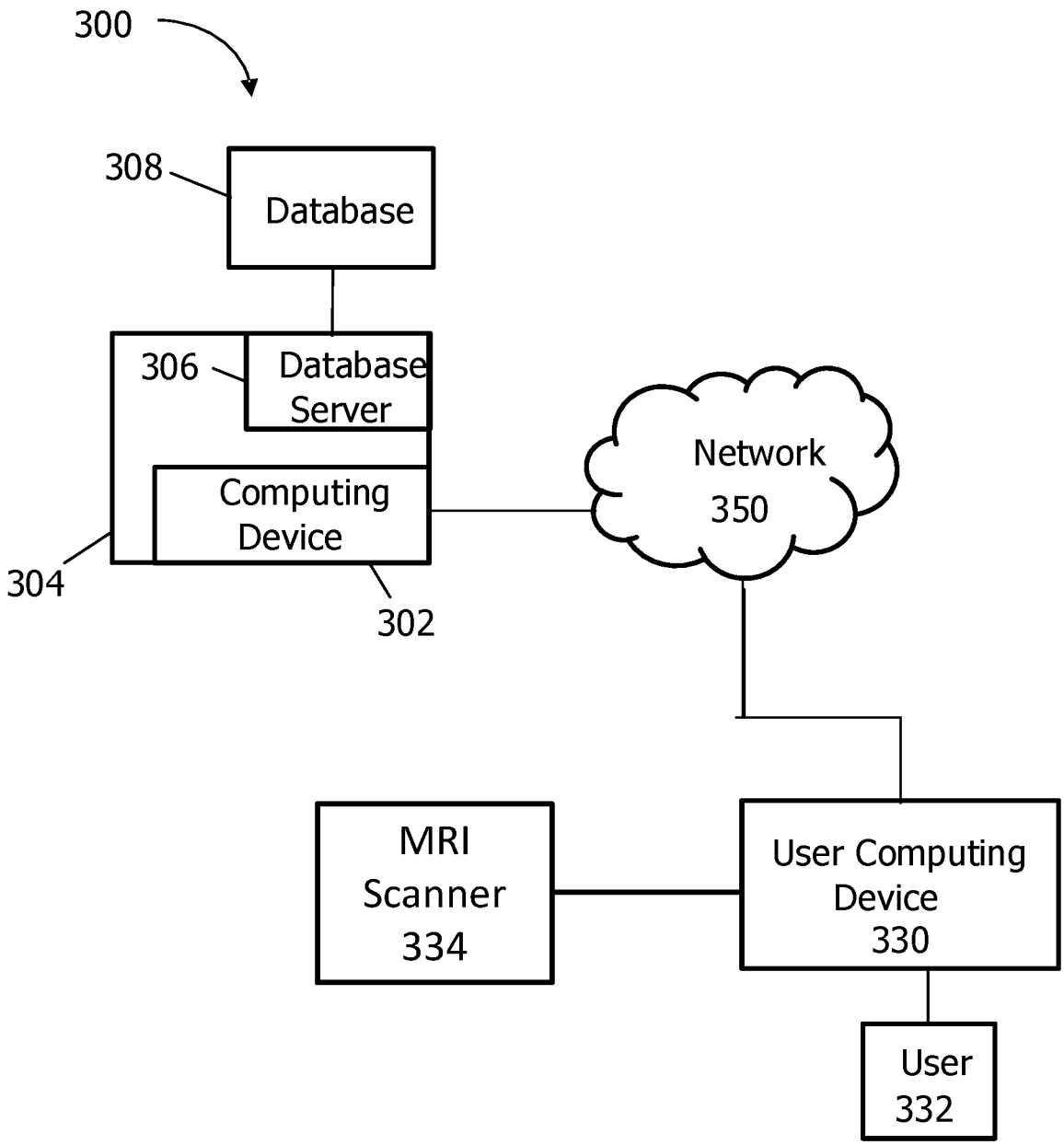
300
308
Database
306
Database Server
Computing Device
304
302
Network
350
MRI Scanner
334
User Computing Device
330
User
332

FIG. 1

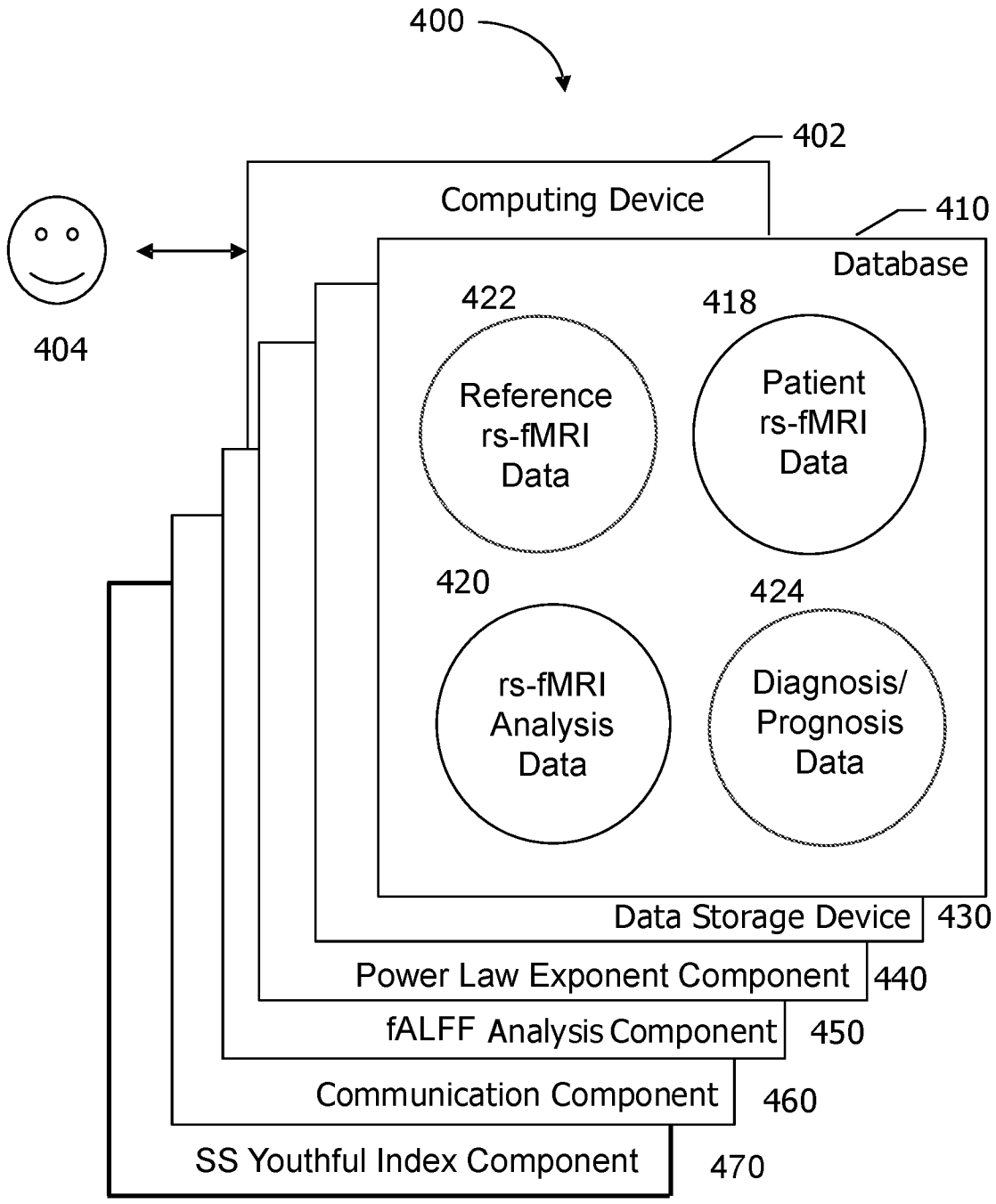
400
402
Computing Device
410
Database
422
Reference rs-fMRI Data
418
Patient rs-fMRI Data
420
rs-fMRI Analysis Data
424
Diagnosis/ Prognosis Data
404
Data Storage Device
430
Power Law Exponent Component
440
fALFF Analysis Component
450
Communication Component
460
SS Youthful Index Component
470

FIG. 2

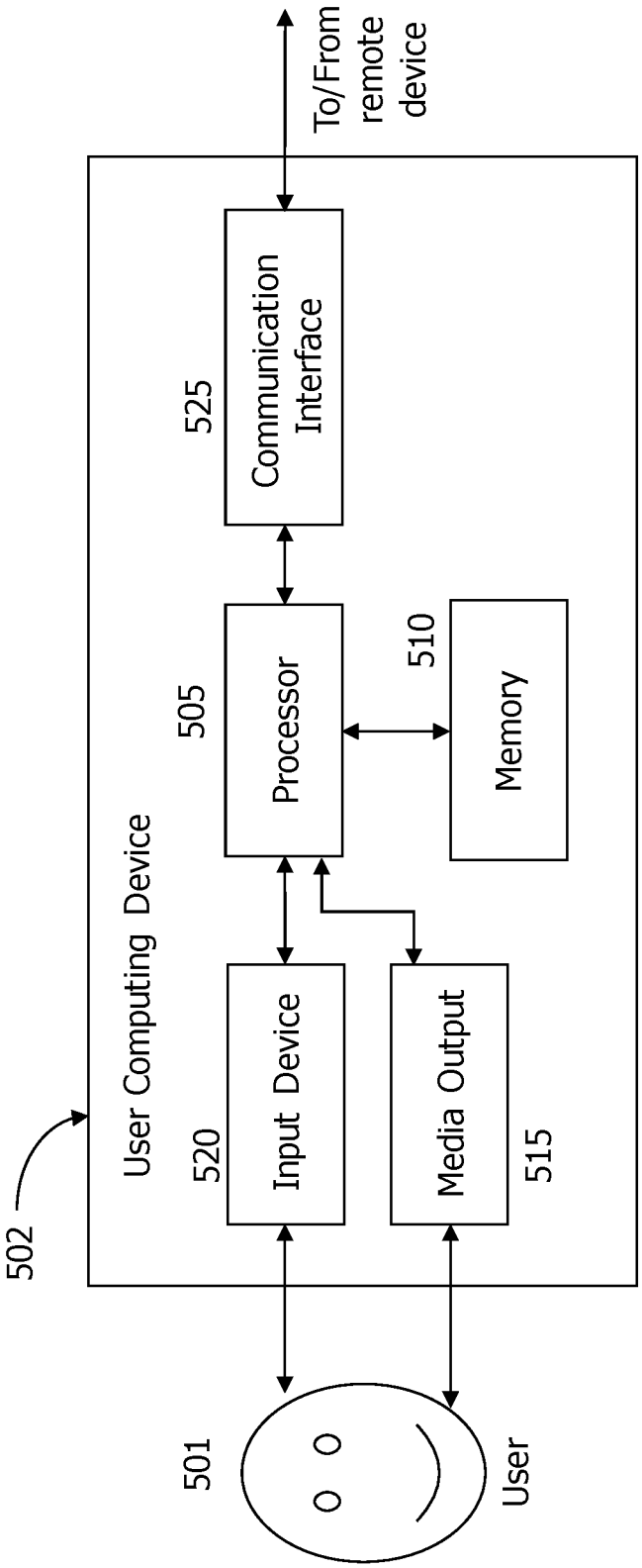
To/From remote device
525
Communication Interface
505
Processor
510
Memory
User Computing Device
520
Input Device
Media Output
515
502
501
User

FIG. 3

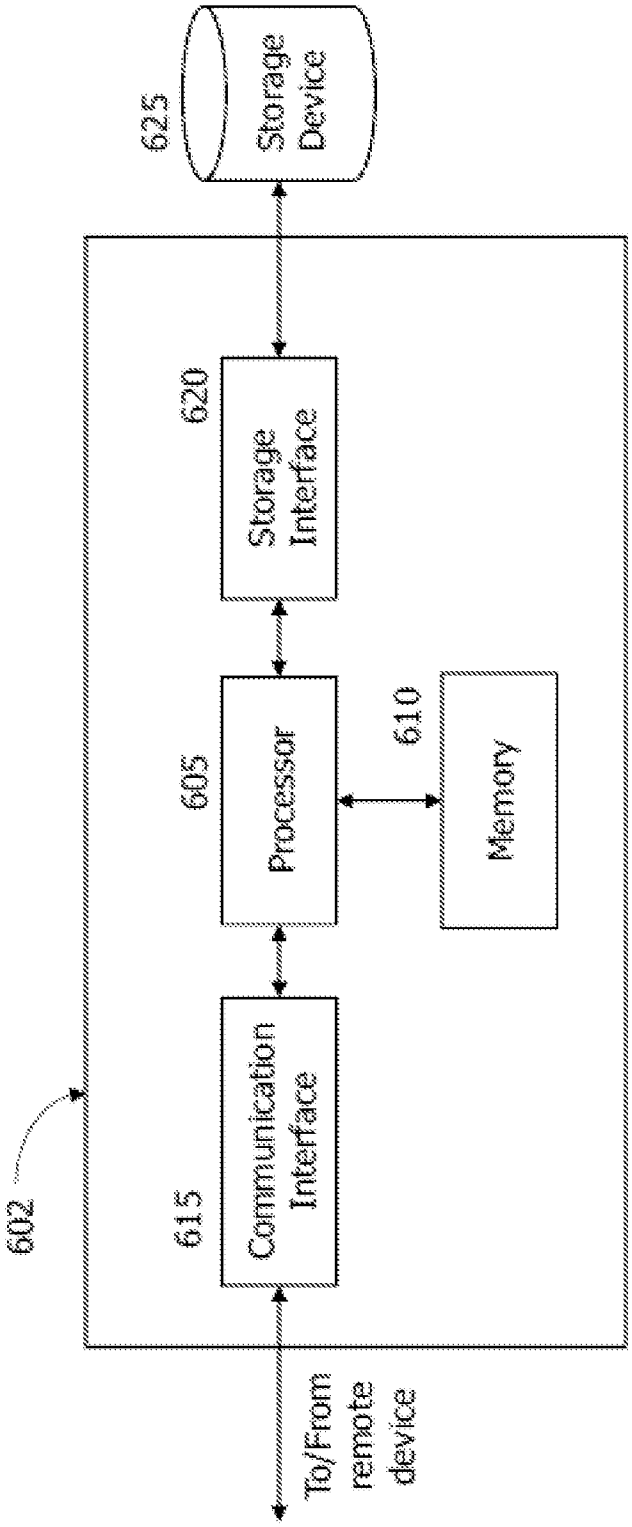
625
Storage Device
620
Storage Interface
605
Processor
610
Memory
615
Communication Interface
602
To/From remote device

FIG. 4

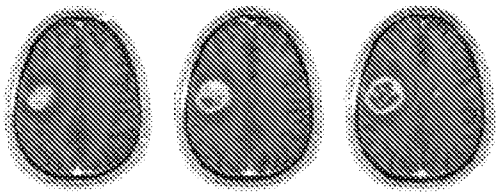

FIG. 5A

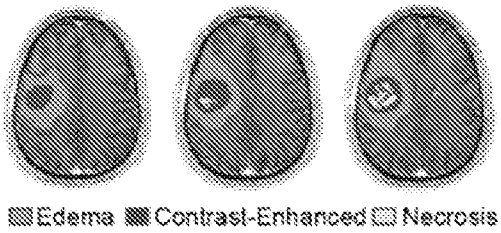

FIG. 5B

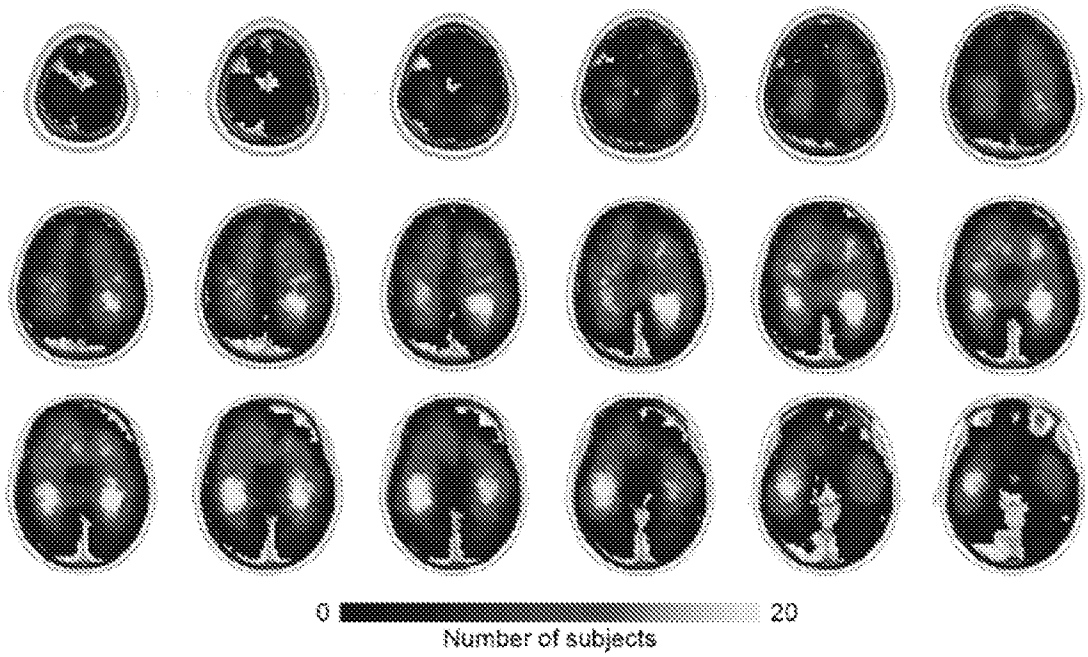

FIG. 5C

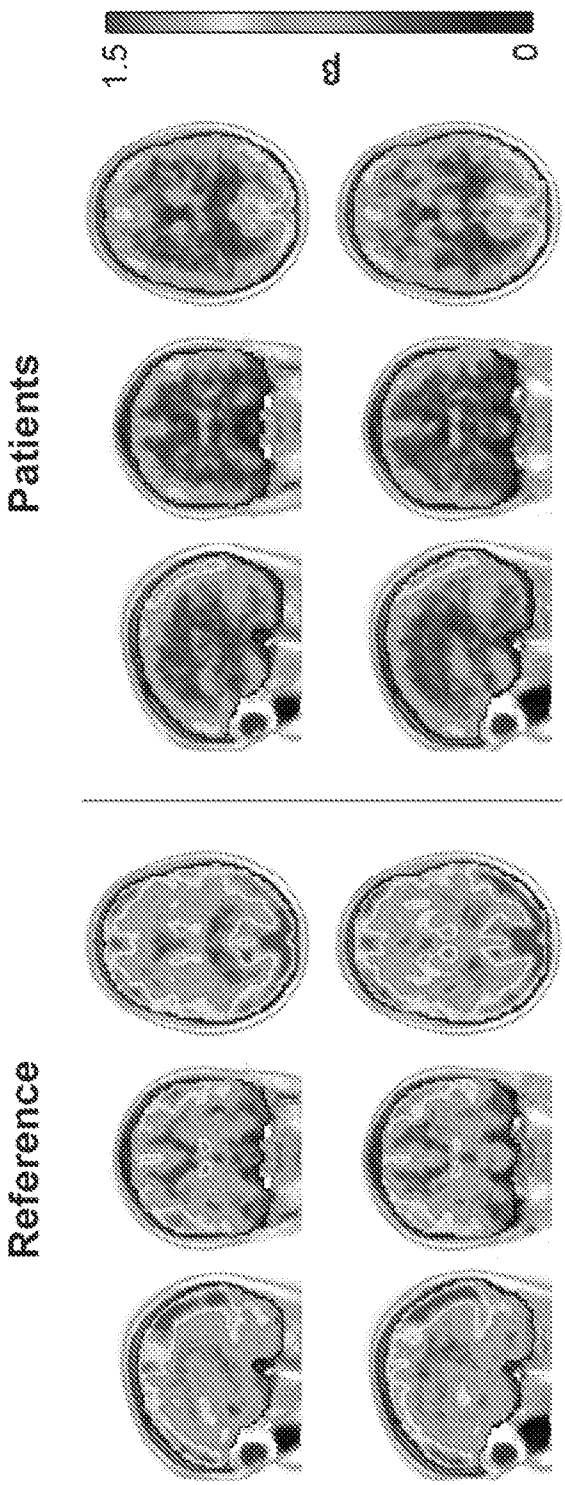

FIG. 6A

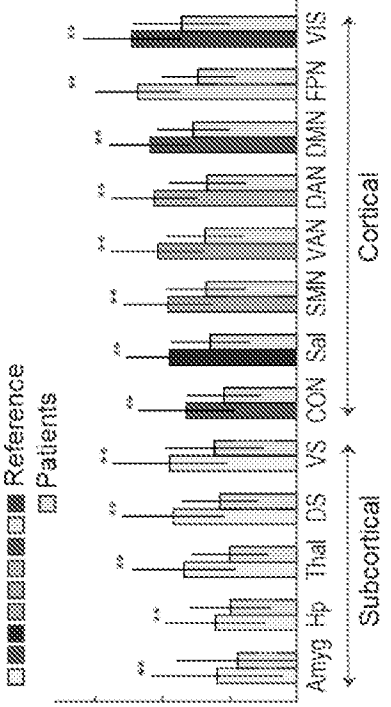

FIG. 6C

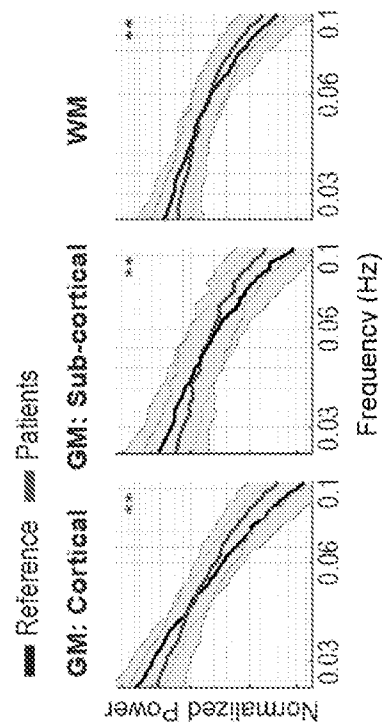

FIG. 6B

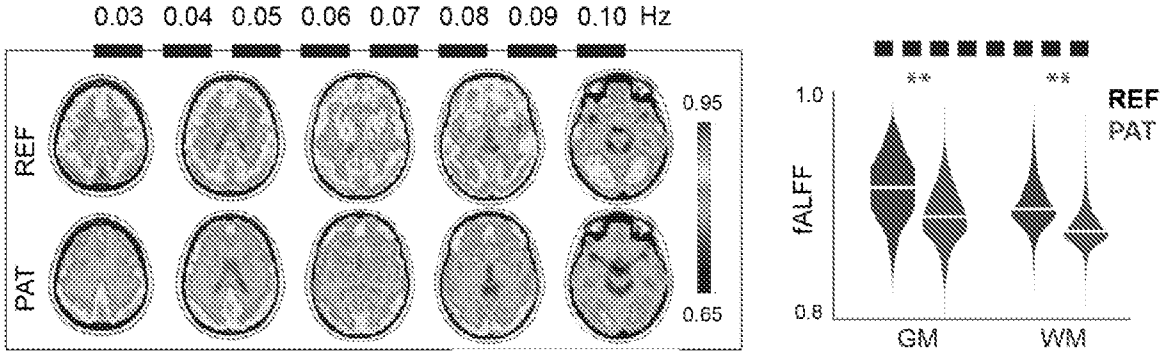

FIG. 7A

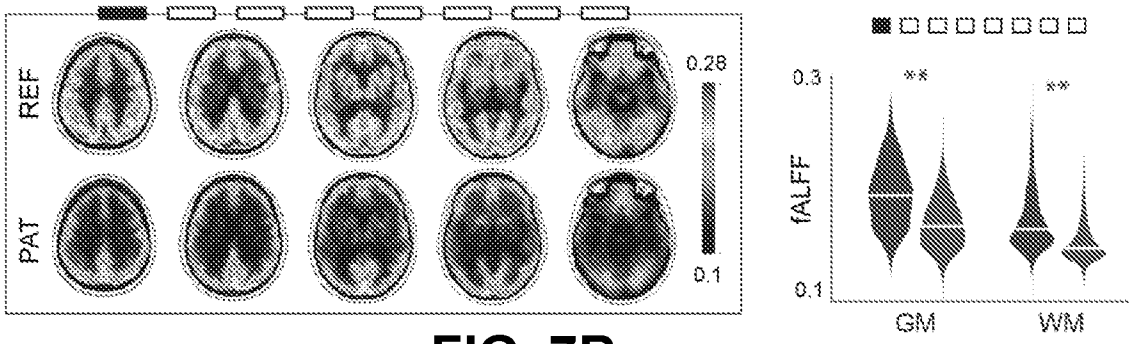

FIG. 7B

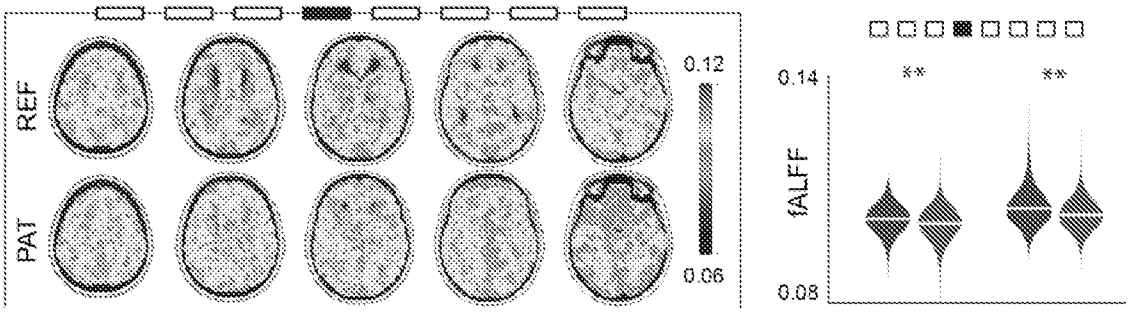

FIG. 7C

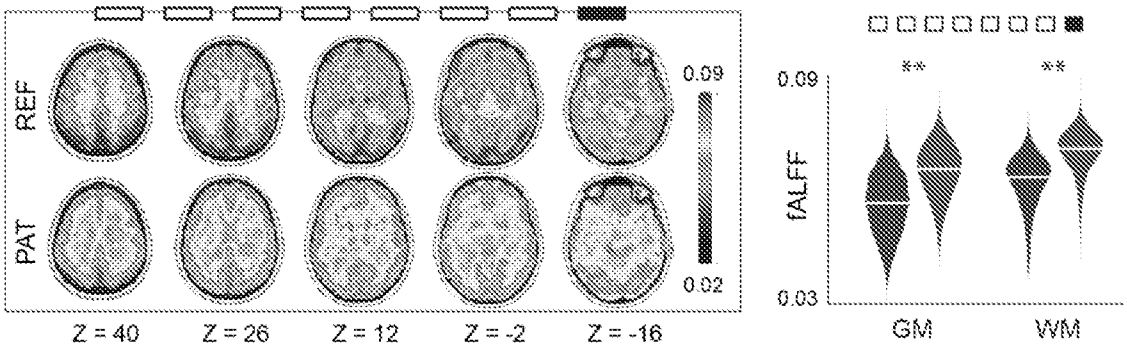

FIG. 7D

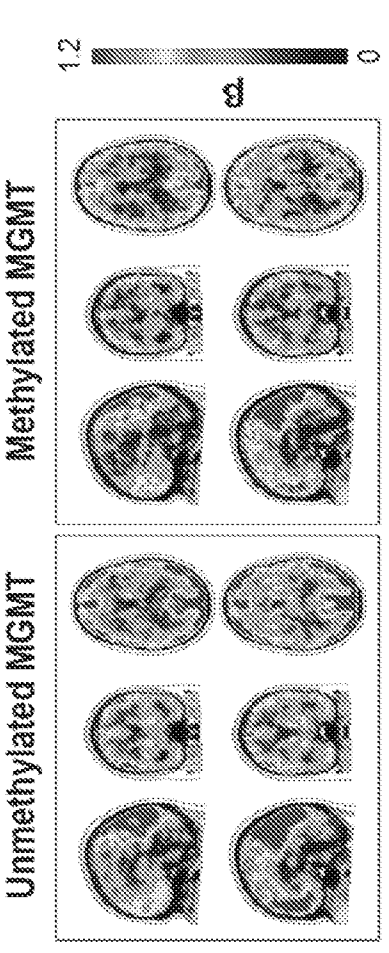

FIG. 8A

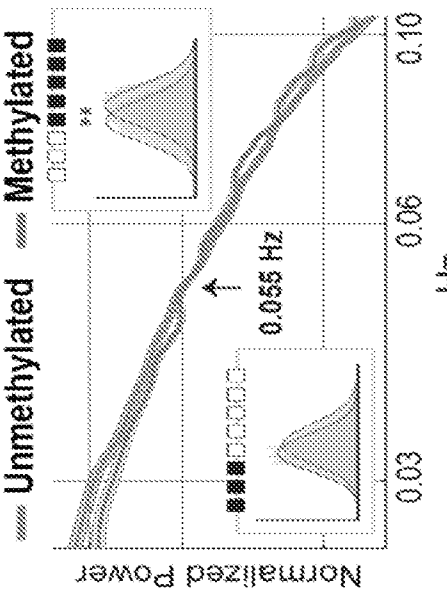

FIG. 8B

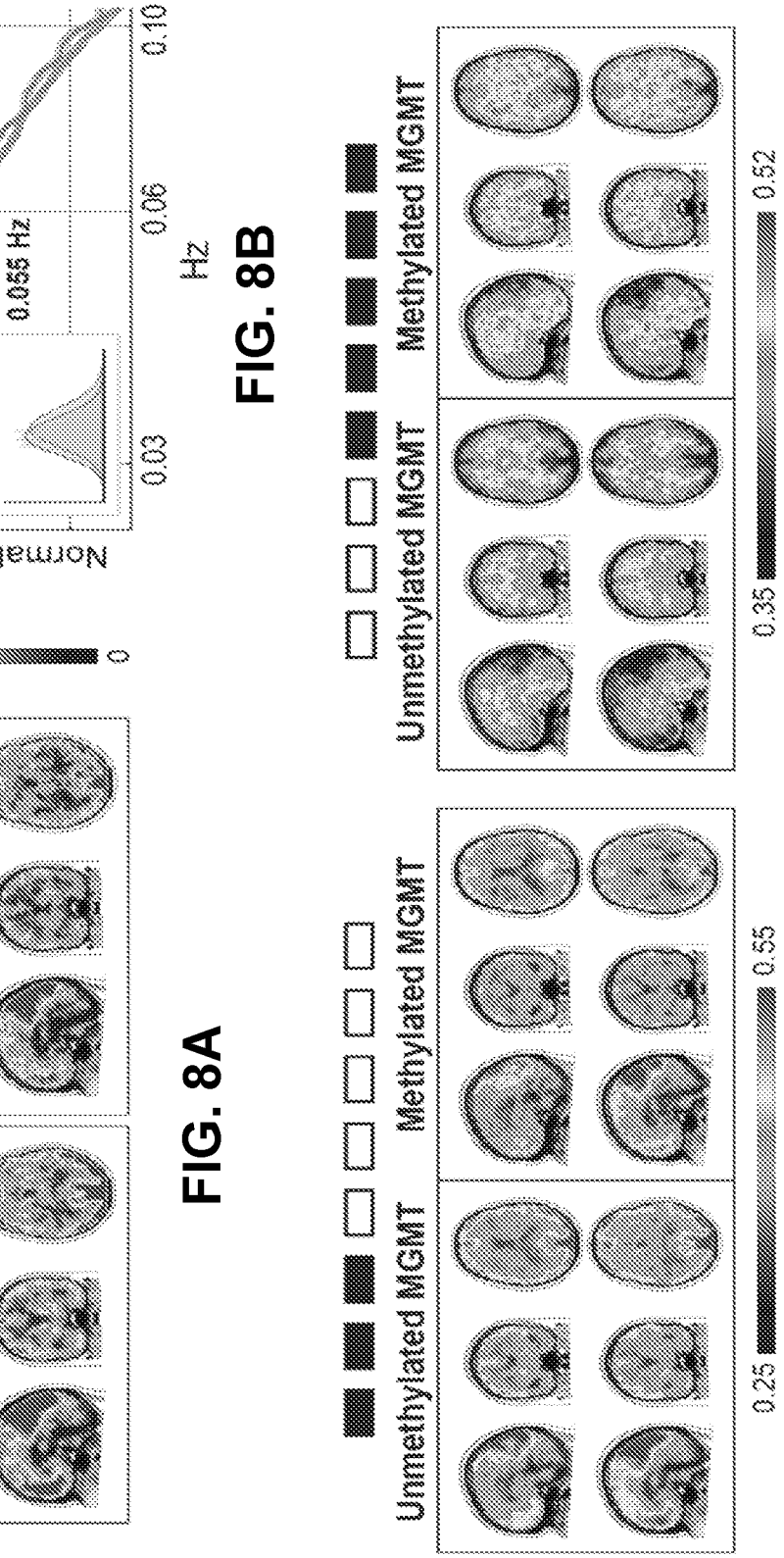

FIG. 8C

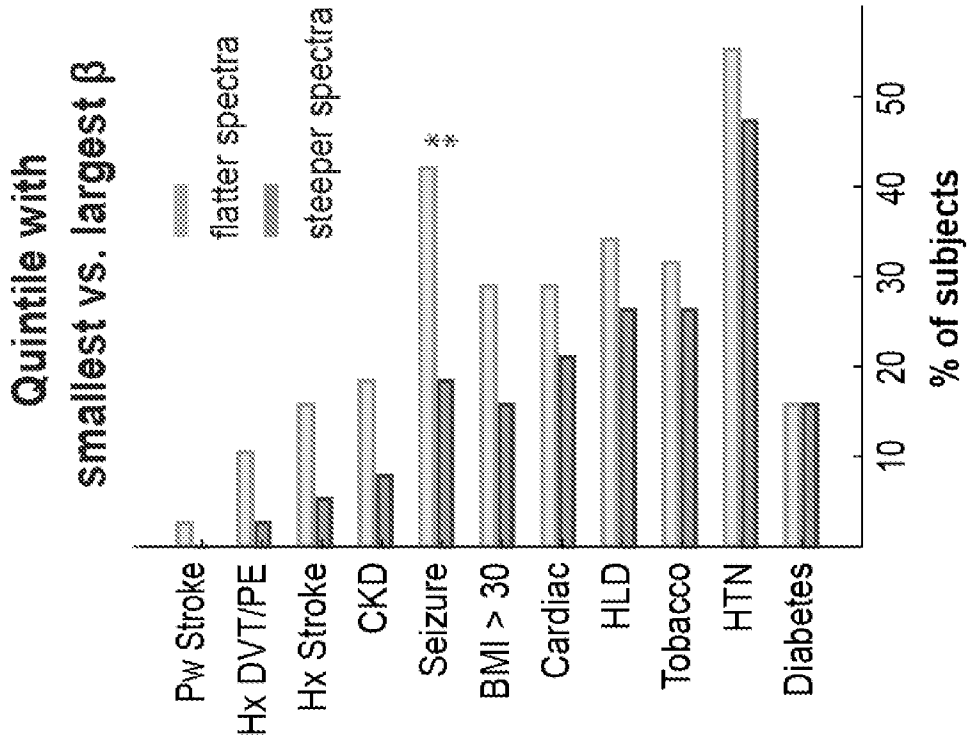
Quintile with
smallest vs. largest β
flatter spectra
steeper spectra
Pw Stroke
Hx DVT/PE
Hx Stroke
CKD
Seizure
BMI > 30
Cardiac
HLD
Tobacco
HTN
Diabetes
**
10
20
30
40
50
% of subjects

FIG. 9A

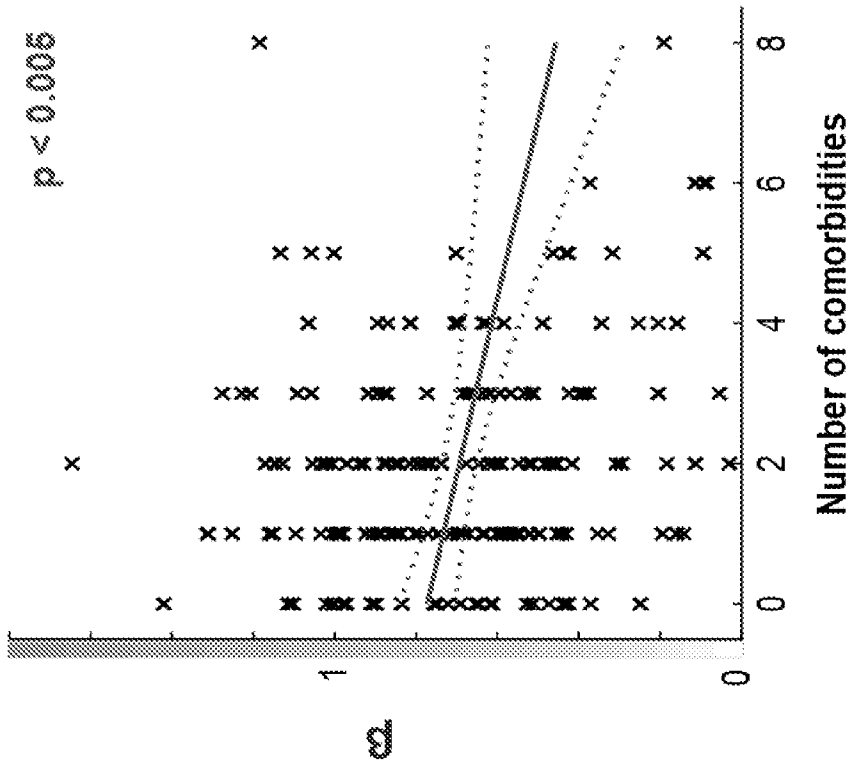
Number of comorbidites vs β
p < 0.005
β
1
0
0
2
4
6
8
Number of comorbidities

FIG. 9B

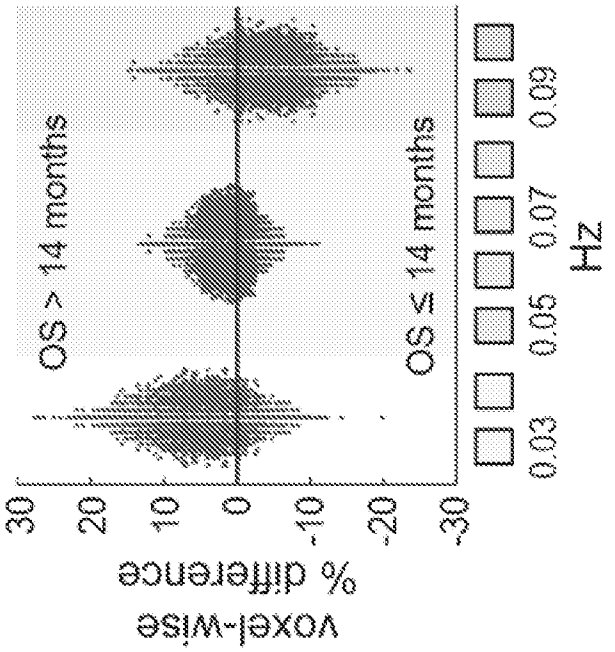

FIG. 10B

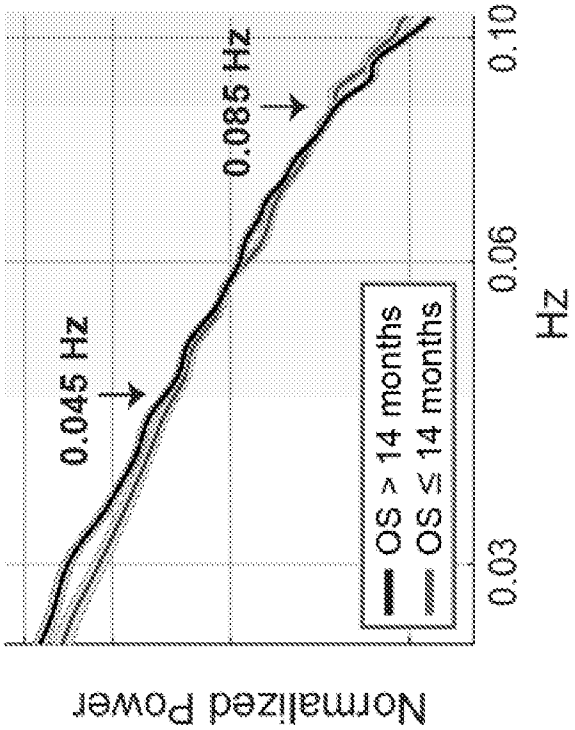

FIG. 10A

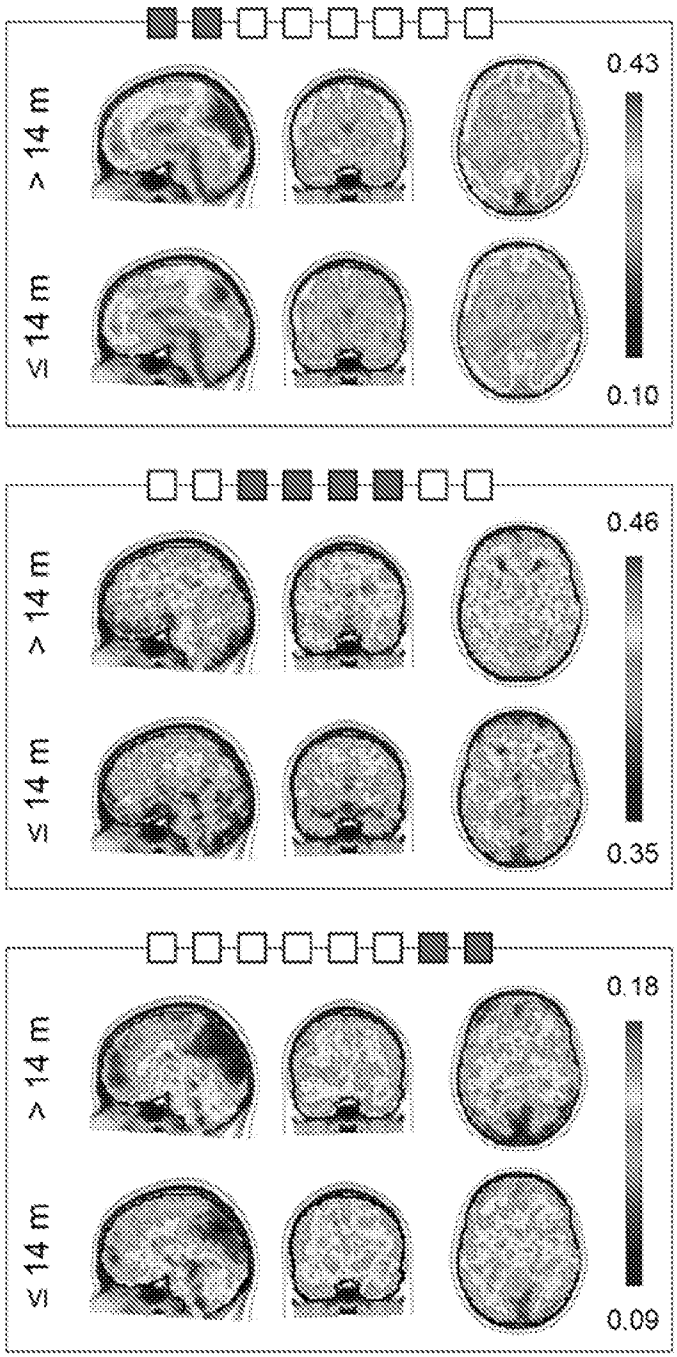

FIG. 10C

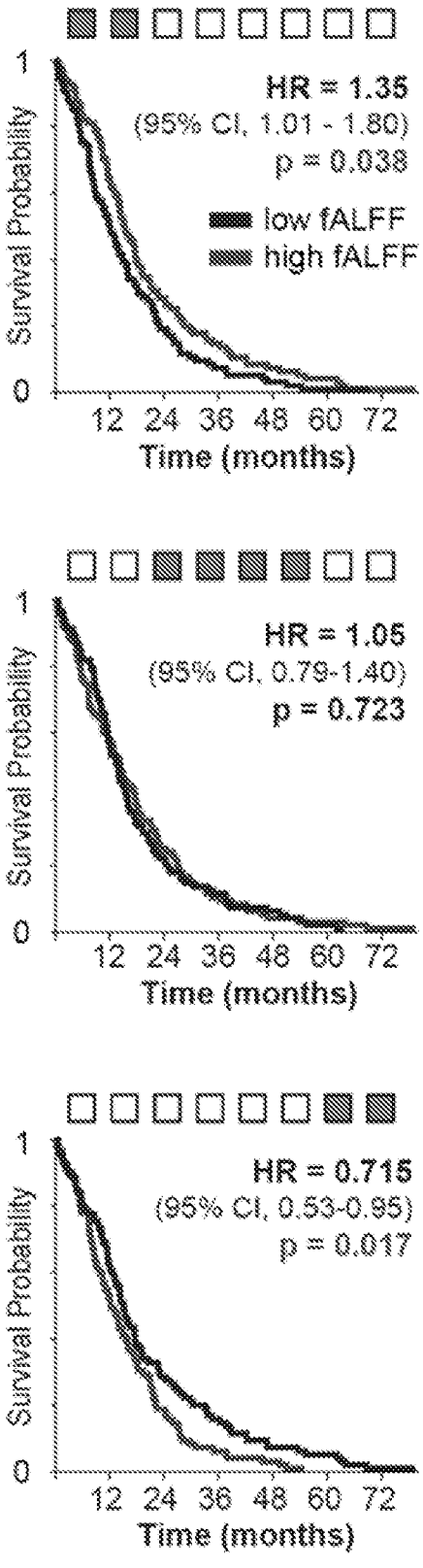
HR = 1.35
(95% CI, 1.01 - 1.80)
p = 0.038
low fALFF
high fALFF
Survival Probability
1
0
12 24 36 48 60 72
Time (months)
HR = 1.05
(95% CI, 0.79-1.40)
p = 0.723
Survival Probability
1
0
12 24 36 48 60 72
Time (months)
HR = 0.715
(95% CI, 0.53-0.95)
p = 0.017
Survival Probability
1
0
12 24 36 48 60 72
Time (months)

FIG. 10D

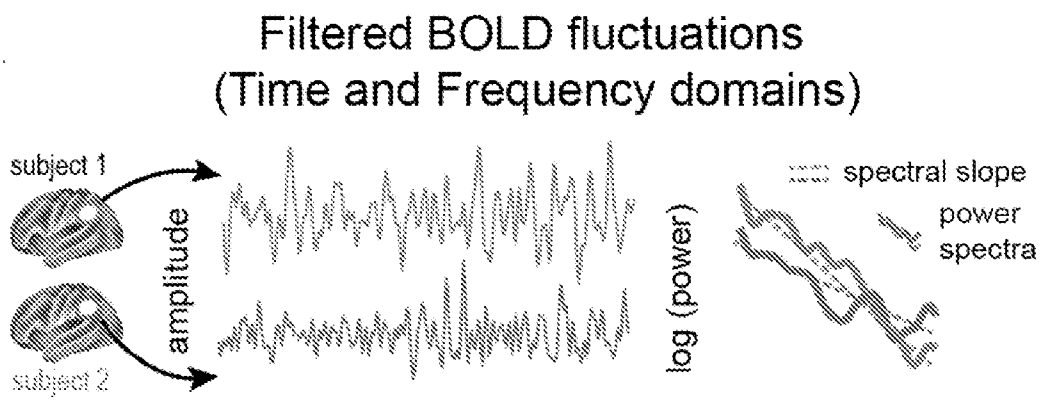

FIG. 11A

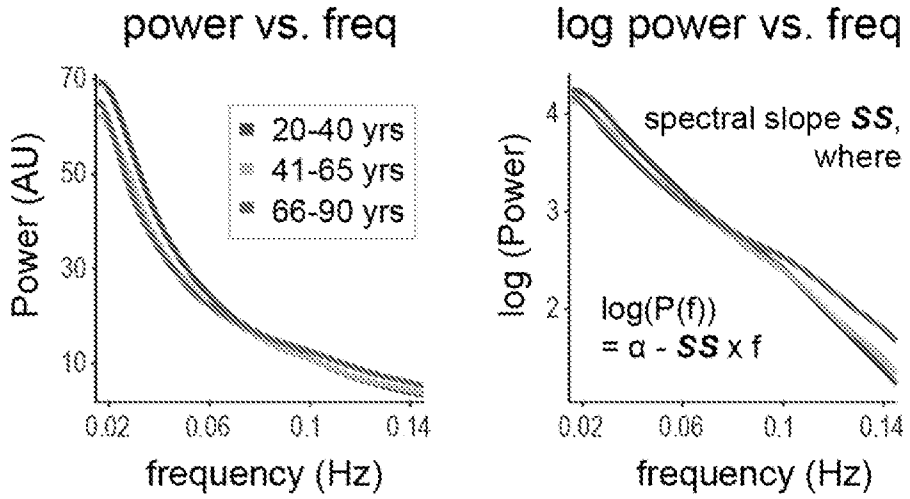

FIG. 11B

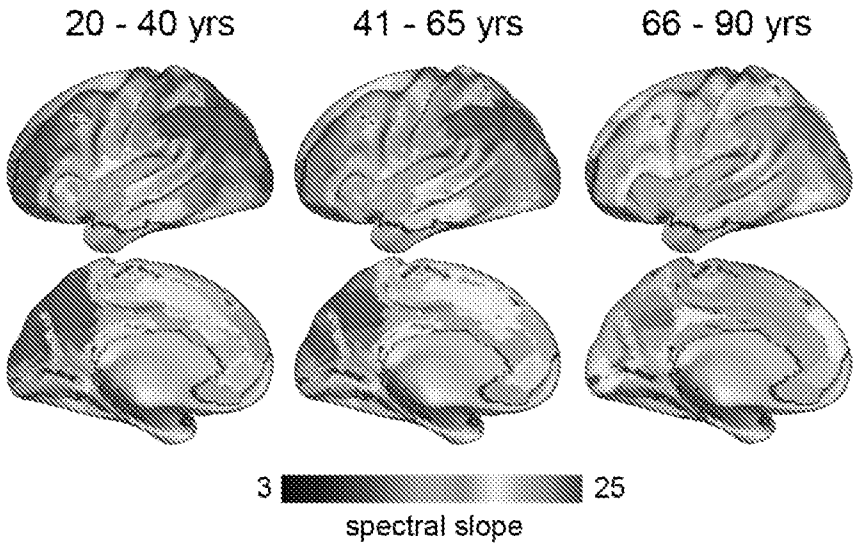

FIG. 11C

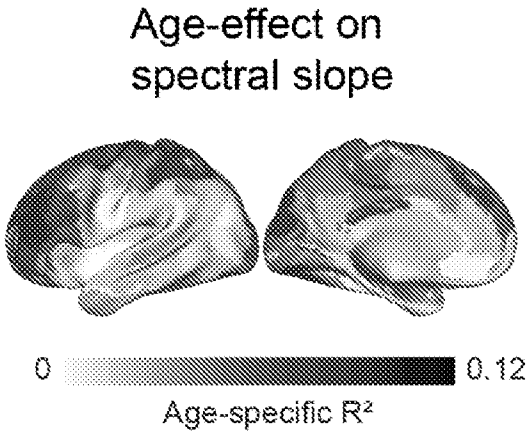

FIG. 12A

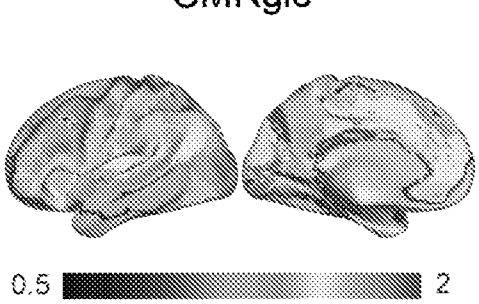

FIG. 12B

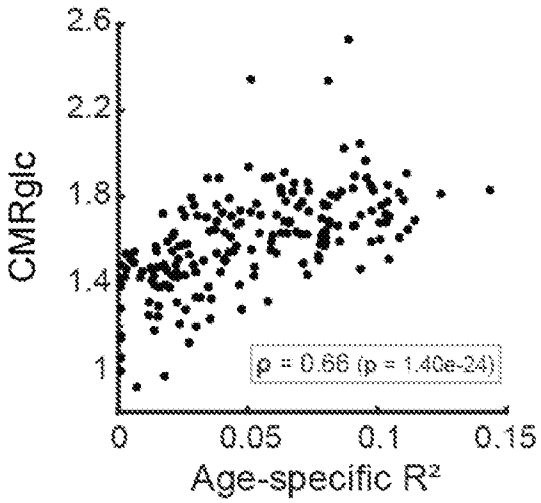

FIG. 12C

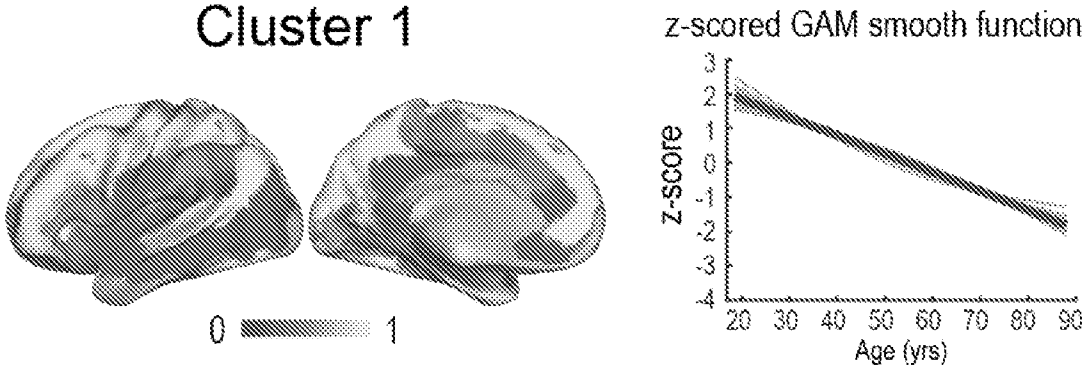

FIG. 13A

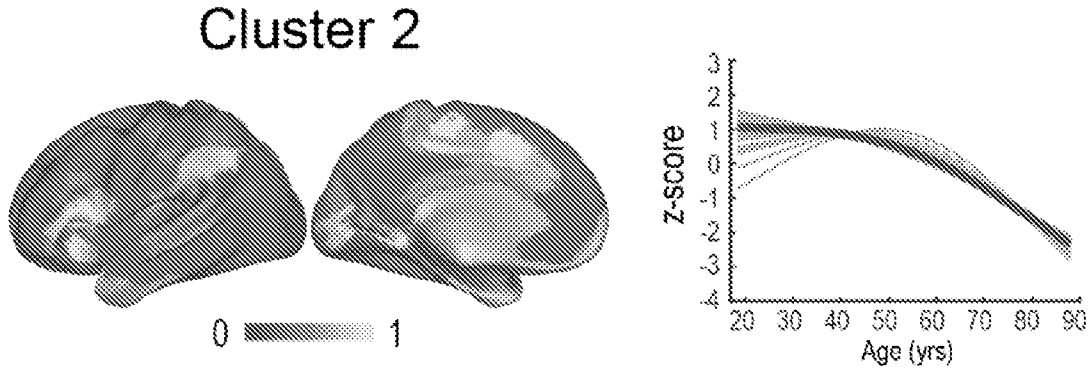

FIG. 13B

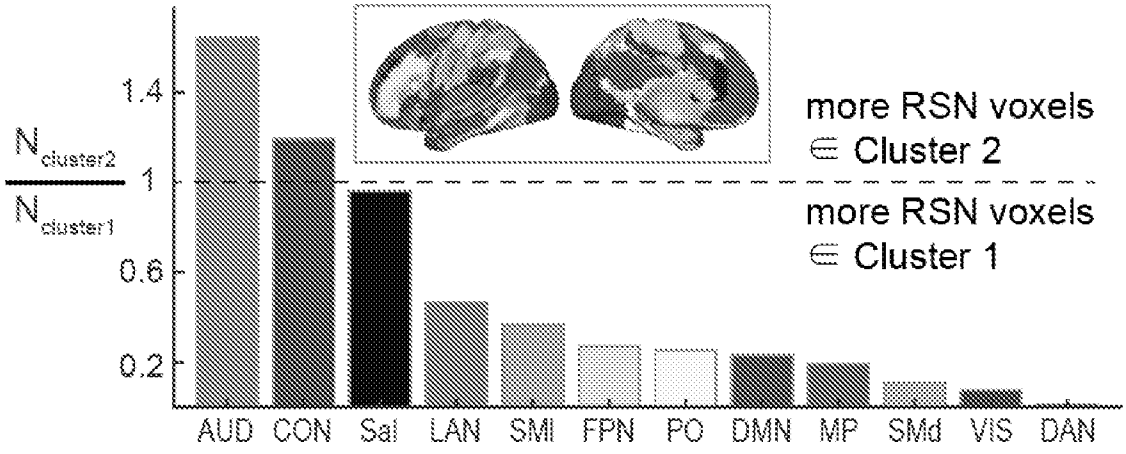

FIG. 13C

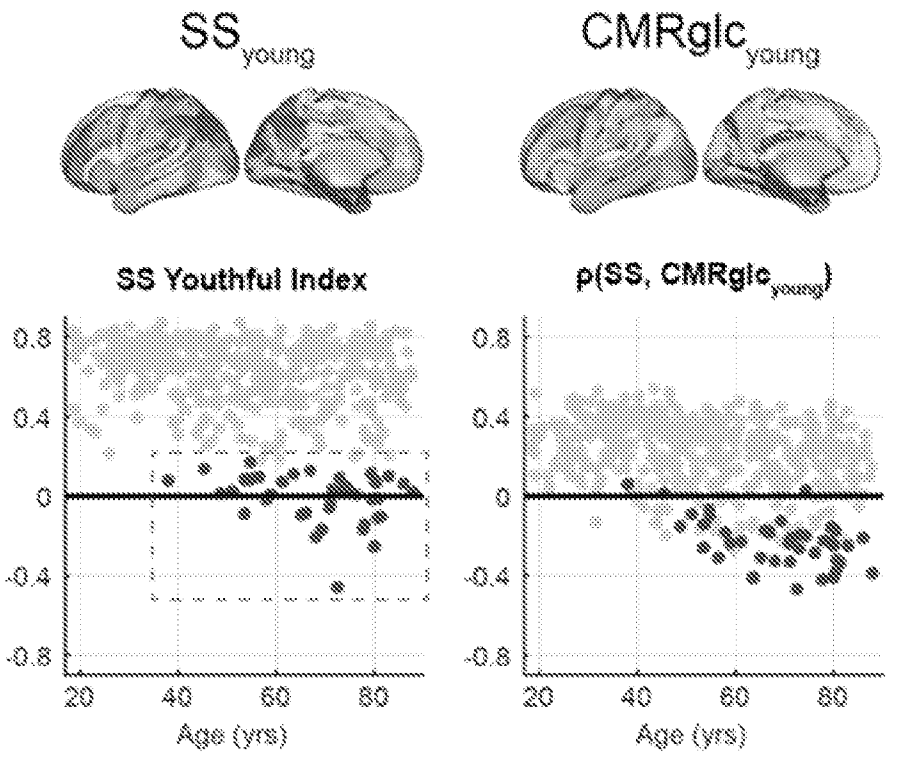

FIG. 14A

FIG. 14B

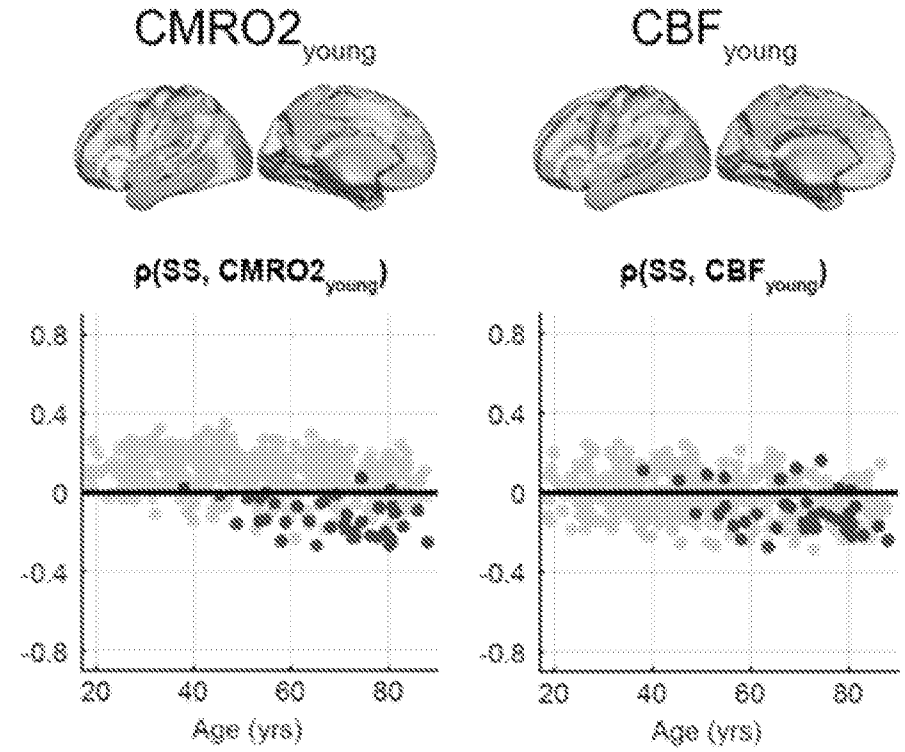

FIG. 14C

FIG. 14D

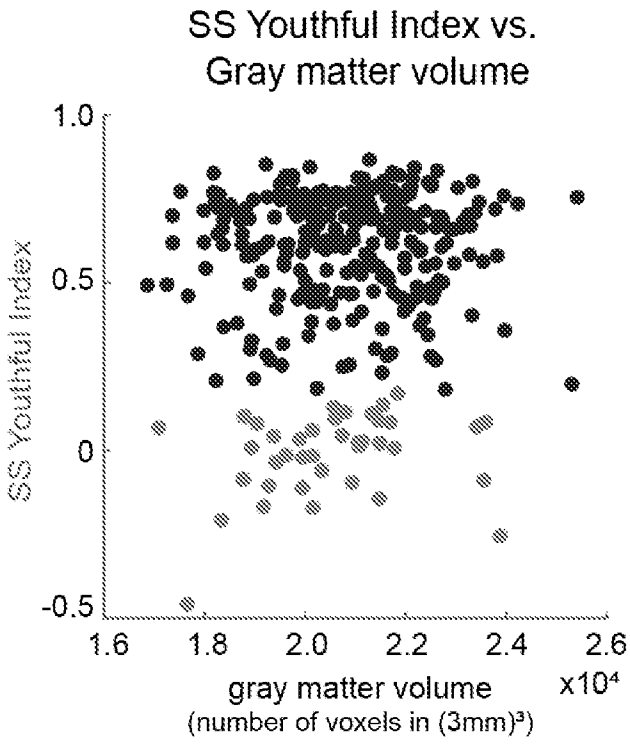

FIG. 15A

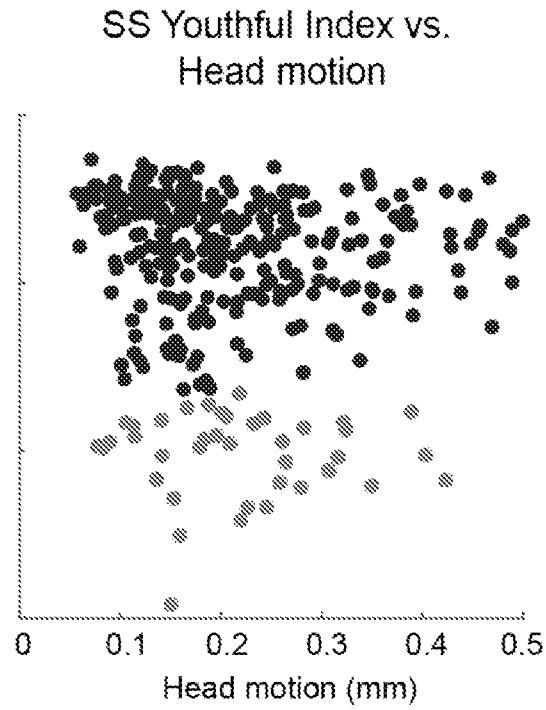

FIG. 15B

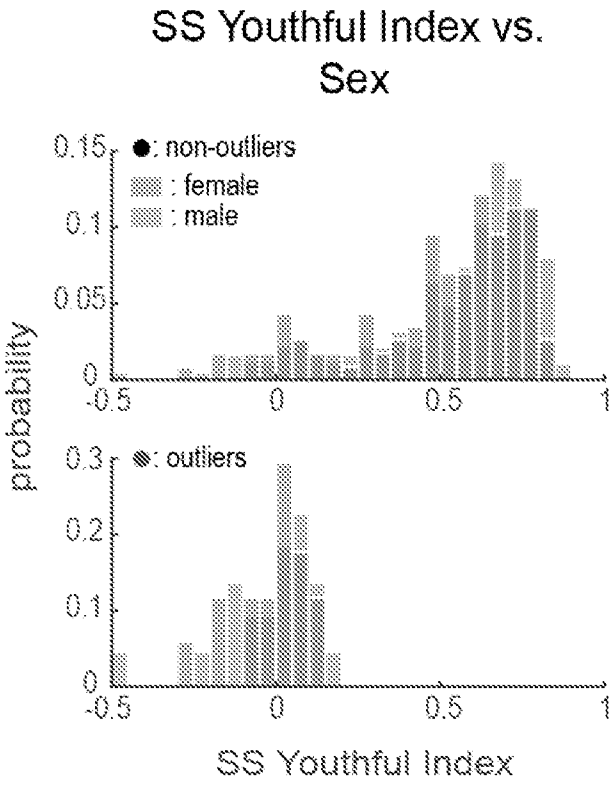

FIG. 15C

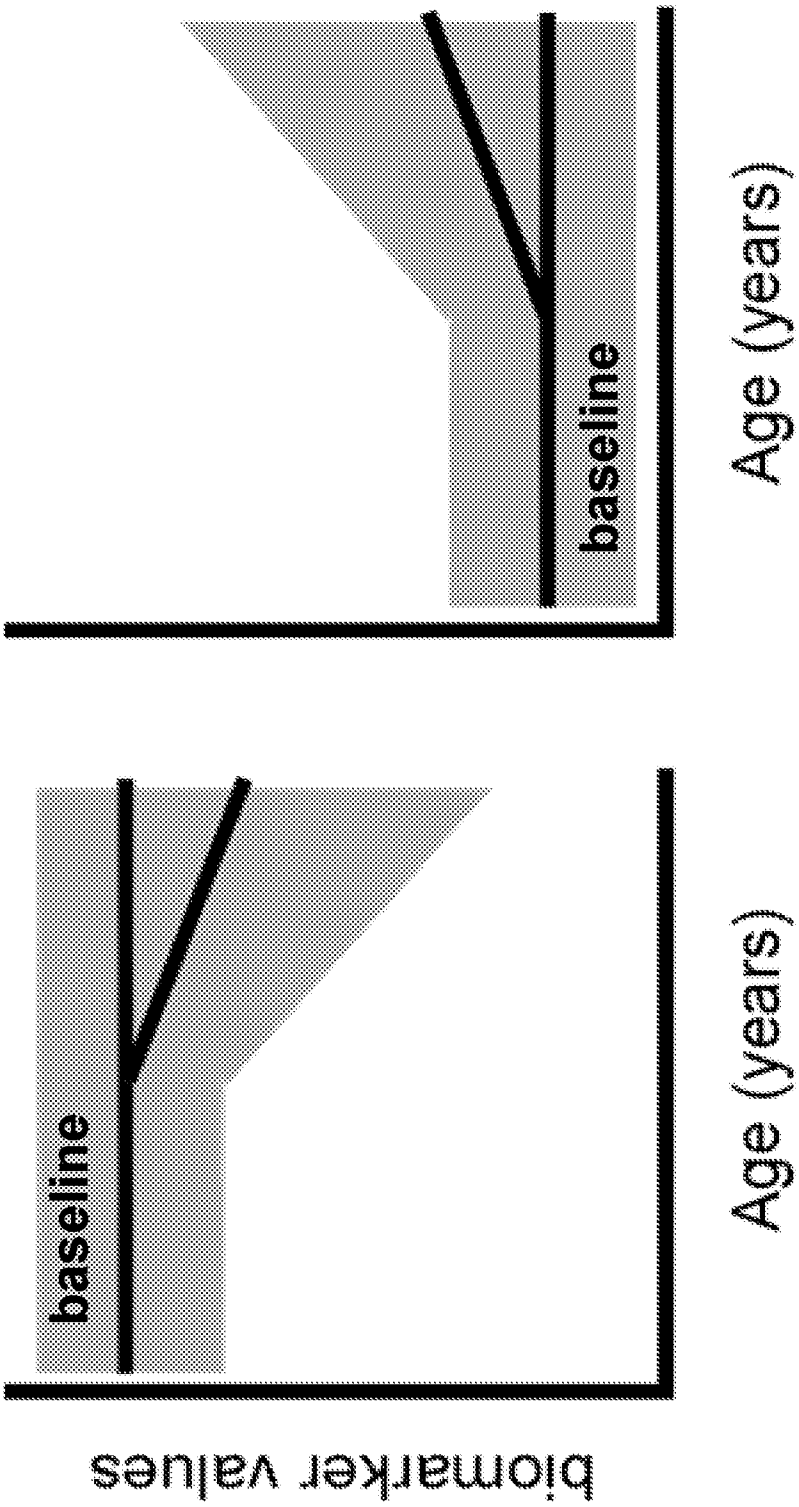

FIG. 16

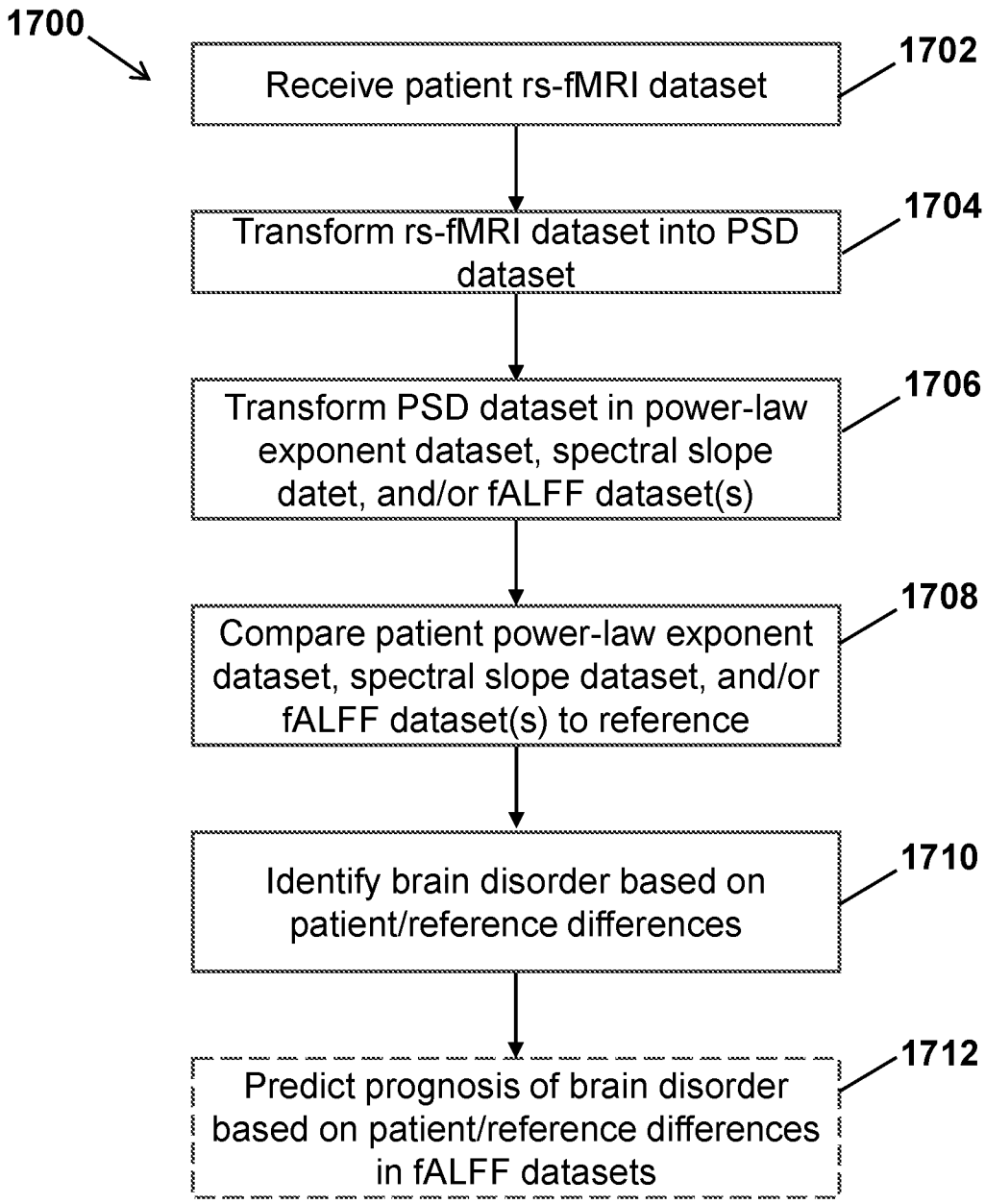
1700
Receive patient rs-fMRI dataset
1702
Transform rs-fMRI dataset into PSD dataset
1704
Transform PSD dataset in power-law exponent dataset, spectral slope datet, and/or fALFF dataset(s)
1706
Compare patient power-law exponent dataset, spectral slope dataset, and/or fALFF dataset(s) to reference
1708
Identify brain disorder based on patient/reference differences
1710
Predict prognosis of brain disorder based on patient/reference differences in fALFF datasets
1712

FIG. 17

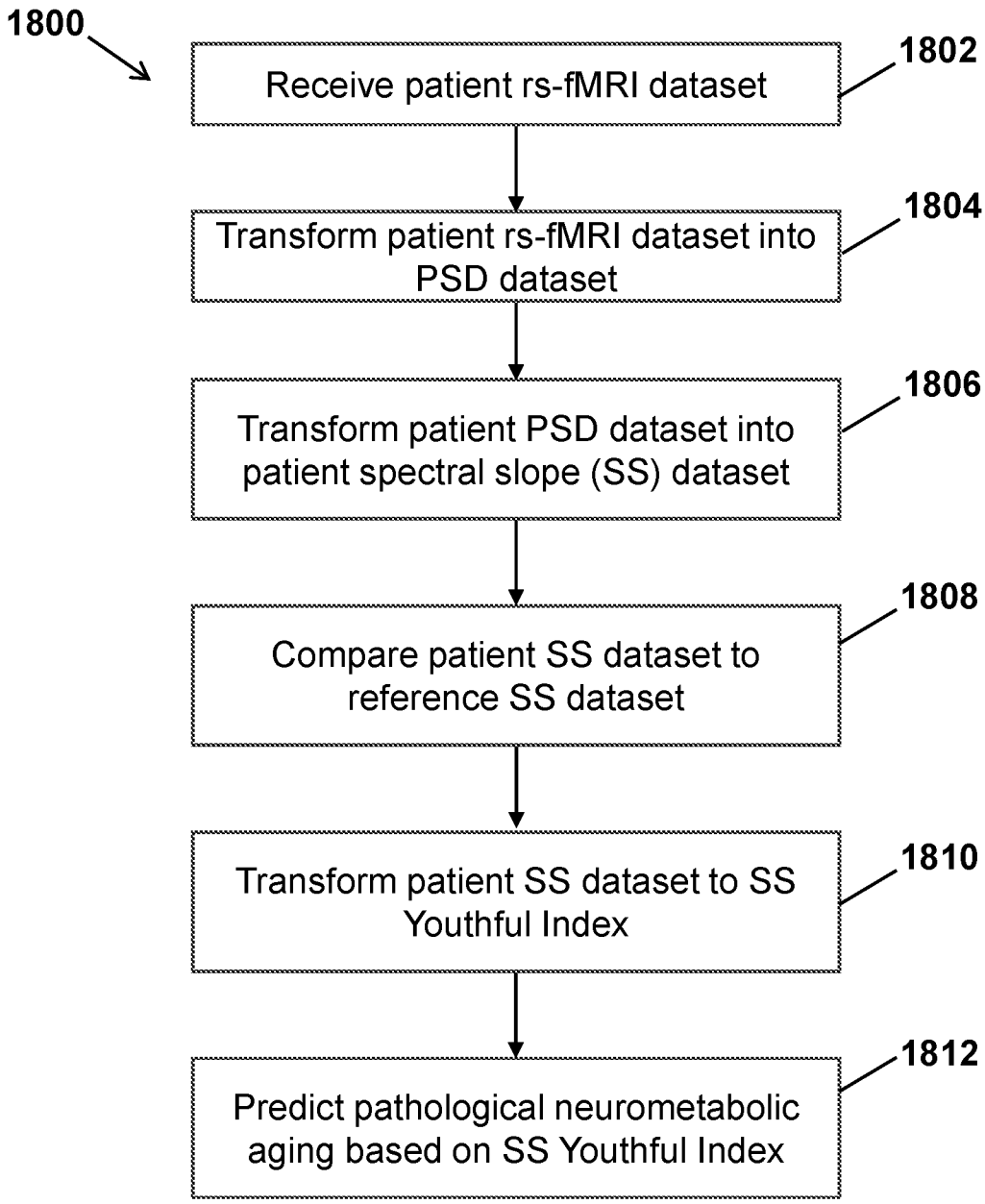
1800
Receive patient rs-fMRI dataset
1802
Transform patient rs-fMRI dataset into PSD dataset
1804
Transform patient PSD dataset into patient spectral slope (SS) dataset
1806
Compare patient SS dataset to reference SS dataset
1808
Transform patient SS dataset to SS Youthful Index
1810
Predict pathological neurometabolic aging based on SS Youthful Index
1812

FIG. 18